Emulating galaxy clustering and galaxy-galaxy lensing into the deeply nonlinear regime: methodology, information, and forecasts

Benjamin D. Wibking[1]⋆, Andrés N. Salcedo[1], David H. Weinberg[1],
Lehman H. Garrison,[2] Douglas Ferrer[2], Jeremy Tinker[3], Daniel Eisenstein[2],
Marc Metchnik[4], and Philip Pinto[4]

[1]*Dept. of Astronomy and Center for Cosmology and AstroParticle Physics, Ohio State University, 140 W 18th Ave, Columbus, OH, USA*

[2]*Harvard-Smithsonian Center for Astrophysics, 60 Garden St., MS-10, Cambridge, MA 02138*

[3]*Center for Cosmology and Particle Physics, New York University, 4 Washington Place, New York, NY 10003*

[4]*Steward Observatory, University of Arizona, 933 N. Cherry Ave., Tucson, AZ 85121*

ABSTRACT

The combination of galaxy-galaxy lensing (GGL) with galaxy clustering is one of the most promising routes to determining the amplitude of matter clustering at low redshifts. We show that extending clustering+GGL analyses from the linear regime down to $\sim 0.5\,h^{-1}$ Mpc scales increases their constraining power considerably, even after marginalizing over a flexible model of non-linear galaxy bias. Using a grid of cosmological N-body simulations, we construct a Taylor-expansion emulator that predicts the galaxy autocorrelation $\xi_{\mathrm{gg}}(r)$ and galaxy-matter cross-correlation $\xi_{\mathrm{gm}}(r)$ as a function of σ_8, Ω_m, and halo occupation distribution (HOD) parameters, which are allowed to vary with large scale environment to represent possible effects of galaxy assembly bias. We present forecasts for a fiducial case that corresponds to BOSS LOWZ galaxy clustering and SDSS-depth weak lensing (effective source density ~ 0.3 arcmin^{-2}). Using tangential shear and projected correlation function measurements over $0.5 \leq r_p \leq 30\,h^{-1}$ Mpc yields a ~~1.8~~ 1.9% constraint on the parameter combination ~~$\sigma_8 \Omega_m^{0.58}$~~ $\sigma_8 \Omega_m^{0.61}$, a factor of two better than a constraint that excludes non-linear scales ($r_p > 2\,h^{-1}$ Mpc, $4\,h^{-1}$ Mpc for γ_t, w_p). Much of this improvement comes from the non-linear clustering information, which breaks degeneracies among HOD parameters that would otherwise degrade the inference of matter clustering from GGL. Increasing the effective source density to 3 arcmin^{-2} sharpens the constraint on ~~$\sigma_8 \Omega_m^{0.58}$~~ $\sigma_8 \Omega_m^{0.62}$ by a further factor of two. With robust modeling into the non-linear regime, low-redshift measurements of matter clustering at the 1-percent level with clustering+GGL alone are well within reach of current data sets such as those provided by the Dark Energy Survey.

Key words: cosmology – weak lensing – large scale structure

1 INTRODUCTION

Weak gravitational lensing is the most powerful tool for measuring the clustering of dark matter at low redshifts. Cosmic shear analyses use the correlated ellipticities of lensed galaxies to infer the power spectrum of foreground mass fluctuations. In galaxy-galaxy lensing one correlates a shear map with the distribution of foreground galaxies to infer the galaxy-matter cross-correlation. This cross-correlation probes the halo mass profiles and dark matter environments of different classes of galaxies (e.g., Mandelbaum et al. 2006), a valuable diagnostic of galaxy formation physics. The cross-correlations can be combined with measurements of galaxy clustering to infer the amplitude of matter clustering and thereby test dark energy or modified gravity theories for the origin of cosmic acceleration (Weinberg et al. 2013).

The opportunity is easy to understand at the level of linear perturbation theory, which should describe mat-

⋆ E-mail: wibking.1@osu.edu

ter clustering and galaxy bias on large scales where clustering is weak. In this regime, the galaxy and matter auto-correlations are related by a scale-independent bias factor, $\xi_{gg}(r) = b_g^2 \xi_{mm}(r)$. The galaxy-galaxy lensing (hereafter GGL) signal is proportional to $\Omega_m \xi_{gm}(r) = \Omega_m r_{gm} b_g \xi_{mm}(r)$, where Ω_m is the matter density parameter and the galaxy-matter cross-correlation coefficient r_{gm} is expected to approach one on large scales. Assuming $r_{gm} = 1$, one can combine the GGL and $\xi_{gg}(r)$ measurements to cancel the unknown bias factor b_g and constrain $\Omega_m \sqrt{\xi_{mm}(r)}$. The amplitude of this observable can be summarized by the product $\sigma_8 \Omega_m$, where σ_8 is the rms linear theory matter fluctuation in $8\,h^{-1}$ Mpc spheres. In practice, the best constrained parameter combination differs from $\sigma_8 \Omega_m$ because the value of Ω_m affects the shape of the matter correlation function and because geometric distance factors that enter the lensing signal depend on Ω_m (see discussion in Jain & Seljak 1997 and in section 2.5 below). We illustrate the GGL measurement pictorially in Figure 1. In this paper, we use cosmological N-body simulations and halo occupation distribution (HOD; Berlind & Weinberg 2002) methods to predict galaxy clustering and GGL into the deeply nonlinear regime, where b_g may become scale-dependent and r_{gm} may depart from unity. We illustrate the considerable gains that can be made by exploiting small scale GGL and ξ_{gg} measurements in these analyses.

Several previous studies have investigated the use of HODs or related methods to model GGL and galaxy clustering into the non-linear regime (Yoo et al. 2006; Leauthaud et al. 2011; Cacciato et al. 2012; Yoo & Seljak 2012 analysis to large scales where we can exploit and sharpen the resulting cosmological constraints. These studies have generally relied on analytic approximations with some numerical simulation tests, but the precision of observations has reached the point that the accuracy of the analytic approximations is becoming a limiting factor. Our approach is similar in spirit to the numerically based "emulator" scheme introduced by Heitmann et al. (2009) to predict nonlinear matter power spectra, extended here with HOD parameters. More recently, an emulator approach was used for a cosmological analysis of cluster lensing by Murata et al. (2018). We use a similar approach here with a set of simulations used to predict ξ_{gm} and ξ_{gg}. We ultimately plan to consider a grid of cosmological parameters that spans the space allowed by cosmic microwave background (CMB) data, but in this paper we consider a fiducial cosmology based on Planck CMB results (Planck Collaboration et al. 2016) plus four simulations with fixed steps in σ_8 and Ω_m (at fixed $\Omega_m h^2$). For our fiducial HOD, we consider parameters appropriate to the LOWZ sample of the Baryon Oscillation Spectroscopic Survey (BOSS; Eisenstein et al. 2011; Dawson et al. 2013), as the combination of imaging from the Sloan Digital Sky Survey (SDSS; York et al. 2000) with BOSS LOWZ spectroscopy is one of the most powerful current data sets for clustering and GGL analysis (Singh et al. 2016). Instead of the Gaussian Process emulator of Heitmann et al. (2009), we use a simple linear Taylor expansion in cosmological and HOD parameters. This approach becomes viable when the observational constraints about fiducial parameters are tight, but its adequacy must be tested in the context of any specified data analysis.

HOD methods characterize the relation between galax-

ies and dark matter in terms of the probability $P(N|M_{halo})$ that a halo of mass M_{halo} contains N galaxies of a specified class (Benson et al. 2000). The principal question for cosmological inference from GGL and clustering is whether the adopted HOD parameterization has enough freedom to represent non-linear galaxy bias at the level of accuracy required in order to model the observations. The clustering of dark matter halos depends on their formation history as well as their mass, an effect commonly known as halo assembly bias (Sheth & Tormen 2004; Gao et al. 2005; Harker et al. 2006; Wechsler et al. 2006). Correlations of galaxy properties with halo assembly history at fixed mass can therefore induce galaxy assembly bias, which is not accounted for in traditional HOD parameterizations. Analyzing the mock galaxy catalogs of Hearin & Watson (2013), McEwen & Weinberg (2016) show that even when the model galaxy population has substantial assembly bias, fitting it with a standard HOD yields a cross-correlation coefficient $r_{gm}(r)$ accurate at the ~2 per cent level and thus predicts the correct relative amplitude of galaxy clustering and GGL. In this paper, we explicitly allow for variation of the HOD with large scale environment in our parameterization, as a way of accounting for galaxy assembly bias (see section 2.4).

GGL measurements can be made with the same imaging data sets acquired for cosmic shear analyses, though there are advantages to combining deep imaging data with a spectroscopic survey of galaxies that serve as the lensing sample. Mandelbaum et al. (2013) analyzed galaxy clustering and GGL in the SDSS DR7 (Abazajian et al. 2009) data set, restricting their analysis to large scales where we can expect $r_{gm} = 1$. They found $\sigma_8(\Omega_m/0.25)^{0.57} = 0.80 \pm 0.05$, which can be scaled to the now commonly used parameter $S_8 = \sigma_8(\Omega_m/0.3)^{0.5} = 0.72 \pm 0.05$ (where we ignore the small difference between 0.5 and 0.57 in the exponent). This is lower than the value $S_8 = 0.83 \pm 0.012$ inferred for a ΛCDM model normalized to the Planck 2015 CMB data (Planck Collaboration et al. 2016, Table 4, TT+TE+EE+lowP+lensing column).

Many but not all recent cosmic shear analyses also find low amplitudes for matter clustering compared to the Planck value (e.g. Heymans et al. 2012; Hildebrandt et al. 2017; but see Jee et al. 2016). More et al. (2015) use an analytic HOD-based approach to model clustering of the BOSS CMASS galaxy sample (effective redshift $z = 0.57$) and GGL measurements of CMASS from the 105 deg^2 of overlap between BOSS and the CFHTLens imaging survey (Heymans et al. 2012). Their results are consistent with Planck-normalized ΛCDM predictions, but the errors are fairly large because of the limited overlap area. Most recently, the Dark Energy Survey (DES) Collaboration has derived $S_8 = 0.783^{+0.021}_{-0.025}$ from the combination of clustering, GGL, *and* cosmic shear in their Year 1 data set, weakening but not eliminating the tension with Planck ΛCDM predictions (DES Collaboration et al. 2017, Table II).

Particularly relevant to this paper, Leauthaud et al. (2017) find discrepancies of 20-40 per cent, well above their statistical errors, at scales $r < 10\,h^{-1}$ Mpc between their measurements of GGL for CMASS galaxies (from CFHTLens and SDSS Stripe 82 imaging) and the numerical predictions from Planck-normalized mock catalogs that reproduce observed CMASS galaxy clustering. (However, the authors did not consider an incompleteness of the

galaxy sample that was unexpectedly large or that has a complicated halo mass dependence, or miscentering of central galaxies with respect to the halo centers; see e.g. More et al. 2015 .) The stakes for robust modeling of non-linear galaxy clustering and GGL are therefore high, and the prospects for high-precision measurements over a range of redshifts will grow rapidly with future DES analyses and forthcoming data from the Subaru Hyper-Suprime Camera (HSC) (Aihara et al. 2017).

The next section describes the construction of our emulator, including the simulation suite, our HOD prescription and formulation of assembly bias, and the sensitivity of clustering and GGL observables to parameter variations about our fiducial choices. In section 3, we derive forecasts for constraints on σ_8, Ω_m, and HOD parameters, using covariance matrices appropriate to BOSS LOWZ galaxy clustering and SDSS-depth GGL measurements (Singh et al. 2016). We show how the expected constraints depend on the choice of scales in the galaxy clustering and GGL measurements and on the effective source density of the weak lensing map. In section 4, we discuss the implications of our results and the prospects for applying our methodology to current and near-future data sets.

2 EMULATOR CONSTRUCTION

Our goal is to provide numerically calibrated analytic recipes to compute the real-space matter auto-correlation $\xi_{\rm mm}(r)$, galaxy auto-correlation $\xi_{\rm gg}(r)$, and galaxy-matter cross-correlation $\xi_{\rm gm}(r)$ for cosmological parameters and HOD parameters that are perturbations around a fiducial model. From these one can compute projected observables that are directly measurable in a galaxy redshift survey or weak lensing survey (see section 2.5 below). Our fiducial cosmological parameters, based on the Planck 2015 CMB analysis (Planck Collaboration et al. 2016) are $\Omega_m = 0.3142$, $\Omega_b = 0.0491$, $h = 0.6726$, $n_s = 0.9652$, and a linear theory power spectrum normalization at $z = 0$ of $\sigma_8 = 0.83$. We assume a flat universe with a cosmological constant and three massless neutrino species ($N_{\rm eff} = 3.04$) with zero cosmological neutrino density. In this paper we consider variations of σ_8 and Ω_m, the two parameters that most affect the relative amplitude of galaxy clustering and GGL. When varying Ω_m we hold $\Omega_m h^2$, $\Omega_b h^2$, n_s, and σ_8 fixed.

For fiducial HOD parameters we choose values appropriate to the BOSS LOWZ galaxy sample at median redshift $z = 0.27$ (see section 2.3). Our methods can be readily extended to other galaxy samples and other redshifts chosen on the basis of specified observational data sets.

2.1 Numerical simulations

Our simulation procedures are described in detail by Garrison et al. (2017). They use the ABACUS N-body code (Ferrer et al., in prep.; Metchnik & Pinto, in prep.; see also Metchnik 2009) and initial conditions computed with the configuration-space 2LPT code described by Garrison et al. (2016). The input power spectra were generated by the linear Boltzmann code CAMB (Lewis & Challinor 2011) for redshift $z = 0$ and rescaled by the linear growth factor to the starting redshift $z = 49$.

For the results in this paper, we use the simulations that consist of a fiducial cosmology favored by the Planck 2015 results, two variations in Ω_m (0.2879, 0.3442) at fixed $\Omega_m h^2$, and two variations in σ_8 (0.78, 0.88). All of these simulations use the same phases in their initial conditions in order to minimize cosmic variance in the computation of derivatives (see section 2.5). These simulations have a box size of 720 h^{-1} Mpc, a particle mass of 1.09×10^{10} h^{-1} $M_\odot$ (for the fiducial Ω_m), with 1440^3 particles, and a Plummer softening length of 41 h^{-1} kpc. We use the particle outputs at redshift $z = 0.3$ in this work, close to the central redshift of BOSS LOWZ (Parejko et al. 2013; Tojeiro et al. 2014). We refer to distances and densities in comoving units throughout this paper.

2.2 Halo identification

We identify halos using the ROCKSTAR halo finder (Behroozi et al. 2013). However, we use strict (i.e., without unbinding) spherical overdensity (SO) halo masses around the halo centers identified with ROCKSTAR, rather than the default 6D FOF-like masses output by ROCKSTAR. For finding halos we use a primary mass definition set to the virial mass of Bryan & Norman (1998), but for all halo masses used after halo finding is complete we adopt the M_{200b} mass definition, i.e., the mass enclosed by a spherical overdensity of 200 times the mean matter density at a given redshift and cosmology. (Isolated halos identified under the virial halo mass definition are not reclassified as subhalos, even though a small fraction of them would not be isolated halos if the halo finder were re-run with the 200b halo mass definition.) Thus, although ROCKSTAR is our identification tool, our eventual halo population consists of dark matter systems with masses and radii defined by the 200ρ_b criterion, effectively centered on local peaks of the dark matter density. We do not make use of dark matter subhalos contained within larger halos, although subhalo masses are always included in parent halo masses.

We have found that the reported concentration parameters ($c = R_{\rm halo}/R_s$ for an NFW profile; Navarro et al. 1997) are not reliable at the mass and force resolution available in our simulations. To obtain concentrations for creating satellite galaxy distributions, therefore, we use the fitting formula of Correa et al. (2015) ,

$$\log c = \alpha + \beta \log M_{\rm halo}[1 + \gamma(\log M_{\rm halo})^2], \tag{1}$$

with parameters $\alpha(z)$, $\beta(z)$, and $\gamma(z)$ functions of redshift that are calibrated to significantly higher resolution simulations. We perform an approximate rescaling from the halo masses defined by 200 times the critical density (M_{200c}) used there to the M_{200b} definition as employed in this work, multiplying the 200c concentration by $\sqrt{2}$ to obtain an approximate value for the 200b concentration, an approximation to the halo profile rescaling advocated by Hu & Kravtsov (2003) . We have verified that marginalizing over the amplitude, power-law slope of the concentration-mass relation, and a cubic term in the logarithm of halo mass (α, β, and γ in eq. 1) does not affect our cosmological results (see section 3.3 for details).
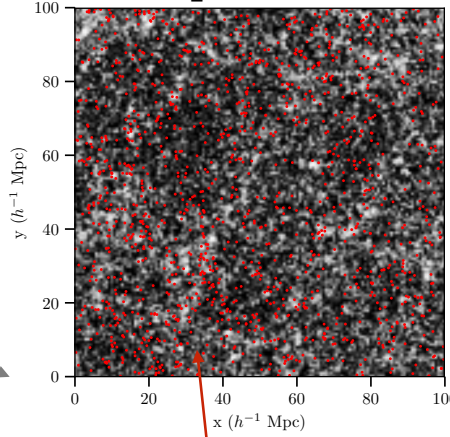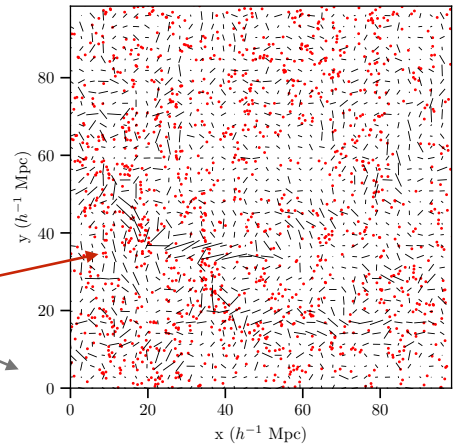
Figure 1. Pictorial illustration of clustering+GGL. The central panel shows the galaxy distribution (red points) and projected matter distribution (grey scale) in a $400\,h^{-1}$ Mpc slice through our fiducial simulation at $z = 0.3$. More distant source galaxies (illustrated here by the Hubble Ultra-Deep Field) are sheared by the intervening dark matter. The cross-correlation of the galaxy distribution and the shear field (shown by lines in the right panel, with arbitrary normalization) is the GGL signal, which can be combined with the galaxy clustering to infer the dark matter clustering at the redshift of the lens population.

2.3 HOD prescription

Our HOD model is similar to that introduced by Zheng et al. (2005) and used in many galaxy clustering analyses (e.g., Zehavi et al. 2005, Zehavi et al. 2011; Coupon et al. 2012; Zu & Mandelbaum 2015). Each halo of a given mass can host central galaxies and satellite galaxies, where hosting satellite galaxies is conditioned on hosting a central galaxy. We compute the expectation value that a given halo will host a central galaxy according to:

$$\langle N_{\text{cen}}|\,M_{\text{halo}}\rangle = \frac{1}{2}\left[1 + \text{erf}\left(\frac{\log M_{\text{halo}} - \log M_{\text{min}}}{\sigma_{\log M}}\right)\right], \qquad (2)$$

where M_{min} is the halo mass for which the occupation probability is one-half, and $\sigma_{\log M}$ allows for logarithmic scatter between galaxy luminosity and halo mass. Throughout this paper we use log for the base-10 logarithm and ln to indicate the natural logarithm. The ~~number of central galaxies is always zero or one, chosen stochastically given the expectation value. The central~~ central galaxy is placed

at the ROCKSTAR-identified halo center, with a weight set according to its expectation value. We compute the expectation value of the number of satellite galaxies according to:

$$\underline{\langle N_{\text{sat}}|\,M_{\text{halo}}, N_{\text{cen}} = 1\rangle}\langle N_{\text{sat}}|\,M_{\text{halo}}\rangle = \begin{cases} \langle N_{\text{cen}}|\,M_{\text{halo}}\rangle\left(\frac{M_{\text{halo}} - M_0}{M_1}\right)^{\alpha} & \text{if } M \\ 0 & \text{oth} \end{cases}$$

$$(3)$$

Here M_0 is a halo mass below which there are no satellite galaxies, $M_1 + M_0$ is the halo mass for which there is an average of one satellite galaxy, and α is the power-law slope of the number of satellites as a function of halo mass. Satellite galaxy counts in a given halo are ~~sampled from~~ assumed to be described by a Poisson distribution with this expectation value ~~to populate individual halos~~, so we weight each point in a cloud of N_{cloud} satellite galaxy sampling points in a given halo according to the ratio $\langle N_{\text{sat}}|\,M_{\text{halo}}\rangle/N_{\text{cloud}}$. We choose N_{cloud} to be at least 10 times the expectation value for a given halo (with a minimum of 5 sampling points per

halo for halos with a nonzero satellite number expectation value). The positions of satellite ~~galaxies~~ galaxy sampling points are chosen by sampling from a satellite galaxy profile:

$$\rho_{\mathrm{sat}}(r) = r^{\Delta\gamma} \rho_{\mathrm{NFW}}(r) , \qquad (4)$$

where $\rho_{\mathrm{NFW}}(r)$ is the NFW density profile with concentration computed from the fitting formula of Correa et al. (2015) and the parameter $\Delta\gamma$ allows a power-law deviation between the satellite galaxy profile and the NFW profile of the mass distribution. We truncate the satellite density profile at the $R_{200,b}$ radius. We note that our weighting scheme based on halo centers and satellite galaxy sampling points is similar to that of Zheng & Guo (2016) , but here we compute all quantities (i.e., correlation functions and number densities) using weights from each halo, rather than computing tables of weights in bins of halo mass.[1]

In an HOD analysis, the number density of galaxies is an important constraint in addition to the galaxy clustering. For our emulator and forecasts, we have elected to take n_{gal} as an HOD parameter in place of M_{min}. Once other parameters have been specified, we use equations 2 and 3 to find the value of M_{min} that yields the specified n_{gal}, keeping the ratios M_0/M_{min} and M_1/M_{min} fixed. The value of M_0/M_{min} is often ill-constrained in HOD fits because it has negligible impact on number density or clustering for $M_0/M_1 \ll 1$. In this paper we have chosen to fix $M_0/M_1 = 0.089$ and not treat it as a free parameter; our results would be negligibly different if we set $M_0 = 0$. (We show that our cosmological constraints are unaffected with respect to allowing M_0/M_1 as a free parameter by additionally computing a variant of the fiducial forecast with M_0/M_1 as a free parameter, as shown in Tables 1 and 2.) Our set of adjustable HOD parameters is therefore n_{gal}, $\sigma_{\log M}$, M_1/M_{min}, α, and $\Delta\gamma$. For our fiducial model we adopt the values $n_{\mathrm{gal}} = 3 \times 10^{-4} \, h^3 \, \mathrm{Mpc}^{-3}$, $\sigma_{\log M} = 0.68$, $M_1/M_{\mathrm{min}} = 9.55$, $\alpha = 1.15$, and $\Delta\gamma = 0$ with the number density based on the LOWZ results of Parejko et al. (2013) and the other parameter values based on the $M_r < -21$ results of Zehavi et al. (2011). We choose the non-number density parameter values from another sample because they are significantly better constrained for the $M_r < -21$ sample but still consistent with the values inferred by modeling by Parejko et al. (2013) of the LOWZ sample itself.

2.4 Modeling galaxy assembly bias

Part of the motivation for HOD descriptions of galaxy bias (see e.g. Berlind & Weinberg 2002) was the expectation from the simplest formulations of excursion set theory (Bond et al. 1991) that halo clustering should be independent of halo formation history at fixed halo mass (White 1994). While this prediction proved a good match to early N-body results (Lemson & Kauffmann 1999), more detailed measurements with larger simulations have revealed a variety of correlations between formation history and halo clustering (e.g., Sheth & Tormen 2004; Gao et al. 2005; Harker et al. 2006;

Wechsler et al. 2006; Salcedo et al. 2017). These correlations can cause the galaxy HOD to vary systematically with halo environment, in which case a calculation that assumes a single global HOD will make incorrect predictions for galaxy clustering and GGL. For example, a model in which galaxy stellar mass is tied to halo peak circular velocity (rather than halo mass) and galaxy color is tied to halo formation time exhibits significant "galaxy assembly bias" for samples defined by luminosity and color cuts; correlation functions change significantly if galaxies are shuffled among halos of the same mass in a way that erases correlations with halo assembly (Zentner et al. 2014).

To allow for assembly bias effects in our HOD model, we have introduced a parameter Q_{env} that shifts the cutoff M_{min} of the central galaxy occupation as a function of the halo's large scale environment. Specifically, we compute the overdensity δ_8 around each halo in a top-hat sphere of radius $8 \, h^{-1}$ Mpc and rank all halos (from 0 to 1) in order of increasing δ_8 in narrow (0.1 dex) bins of halo mass. We then choose an environment-dependent M_{min} for each halo according to

$$\log M_{\mathrm{min}} = \log M_{\mathrm{min},0} + Q_{\mathrm{env}} \left[\mathrm{rank}(\delta_8) - 0.5 \right] , \qquad (5)$$

with a halo at the median overdensity for its mass having $M_{\mathrm{min}} = M_{\mathrm{min},0}$. This prescription is similar to that introduced by McEwen & Weinberg (2016), but using halo rank instead of δ_8 directly makes the result for a given Q_{env} less dependent on the specific choice of environmental variable. It is also fairly intuitive, e.g., for $Q_{\mathrm{env}} = 0.1$ the halos at the environmental extremes have M_{min} across a range of 0.1 dex about that of halos in the median environment. Because we fix M_1/M_{min}, the satellite occupation shifts in $\log M_{\mathrm{halo}}$ together with the central occupation. Although constructed based on the environmental overdensity rather than the concentration parameter of a halo, our parameter has effects on the correlation functions similar to that of the $\mathcal{A}_{\mathrm{cen}}$ parameter considered in Hearin et al. (2016) and used in a clustering analysis of SDSS galaxies by Zentner et al. (2016) .

2.5 Emulated quantities

We use CORRFUNC (Sinha & Garrison 2017) to compute the real-space galaxy autocorrelation ξ_{gg}, galaxy-matter cross-correlation ξ_{gm}, and matter autocorrelation ξ_{mm} on scales $0.01 < r < 125 \, h^{-1}$ Mpc, averaging over 20 realizations of the HOD at each point in parameter space. Separately, we compute the linear matter autocorrelation $\xi_{\mathrm{mm, lin}}$ by computing the appropriate integral over the linear power spectrum used for the initial conditions.

Our emulator uses finite differences to compute a linear Taylor expansion for ratios of these quantities as a function of scale:

$$b_{\mathrm{nl}} = \left[\frac{\xi_{\mathrm{mm}}}{\xi_{\mathrm{mm,lin}}} \right]^{1/2} , \qquad (6)$$

$$b_{\mathrm{g}} = \left[\frac{\xi_{\mathrm{gg}}}{\xi_{\mathrm{mm}}} \right]^{1/2} , \qquad (7)$$

$$r_{\mathrm{gm}} = \left[\frac{\xi_{\mathrm{gm}}^2}{\xi_{\mathrm{gg}} \, \xi_{\mathrm{mm}}} \right]^{1/2} . \qquad (8)$$

---

[1] We note that accumulating pair weights in double precision is critical to obtaining correlation functions that are not dominated by floating point roundoff error.

If needed, we regularize the behavior of these functions on large scales (where the correlation function measurements become noisy) so they obey the expected limits $b_{\rm nl}(r) \to 1$, $b_g(r) \to {\rm const.}$, and $r_{\rm gm}(r) \to 1$ as $r \to \infty$.

We focus on ratios so that the influence of cosmological parameters is treated exactly in the linear regime; there is no need to use a numerical emulator to approximate the impact of parameter changes on the linear matter power spectrum (similar to the methodology of Mandelbaum et al. 2013, who used a linear Taylor expansion in $b_{\rm nl}^2$ in order to model the nonlinear matter correlation function). We expect this approach to give our emulator a wide range of validity, as the scale-dependence of non-linear corrections, galaxy bias, and $r_{\rm gm}(r)$ should have a relatively weak dependence on parameters such as Ω_b, h, and n_s. We will test this expectation using our larger simulation grid in future work, however, we describe a preliminary test based on sampling the posterior parameter space of our fiducial forecast in section 3.3.

Our emulation formula is simply:

$$X(r) = X_{\rm fid}(r) + \sum_i \Delta p_i \frac{\partial X(r)}{\partial p_i} \tag{9}$$

where $X(r)$ may be $\ln b_{\rm nl}(r)$, $\ln b_g(r)$, or $\ln r_{\rm gm}(r)$, $X_{\rm fid}(r)$ is the value in the fiducial model, $\Delta p_i = p_i - p_{i,\rm fid}$ is the difference in parameter i between the emulated model and the fiducial model, and the derivatives are evaluated about the fiducial model. The specific parameters that we use are: $\ln \sigma_8$, $\ln \Omega_m$, $\ln n_{\rm gal}$, $\ln \sigma_{\log M}$, $\ln M_1/M_{\rm min}$, $\ln \alpha$, $\Delta \gamma$, and $Q_{\rm env}$. We generally expect logarithmic derivatives to give a greater range of validity because they can represent power-law relations not just linear relations, but we use linear derivatives for $\Delta \gamma$ and $Q_{\rm env}$ because their fiducial values are zero.

We compute the partial derivatives in equation 9 by centered finite differences with step sizes determined by our set of grid points in cosmological and HOD parameter space. The HOD parameter space used consists of individual parameter variations about the fiducial HOD (evaluated at the fiducial cosmology) at $n_{\rm gal} = \{0.00027, 0.00033\}$, $\sigma_{\log M} = \{0.58, 0.78\}$, $M_1/M_{\rm min} = \{9.05, 10.05\}$, $\alpha = \{1.0, 1.3\}$, $\Delta \gamma = \{-0.1, 0.1\}$ and $Q_{\rm env} = \{-0.1, 0.1\}$. In Appendix B, we tabulate our values of $\xi_{\rm mm,lin}(r)$, $b_{\rm nl,fid}$, $b_{\rm g,fid}$, $r_{\rm gm,fid}$, and the partial derivatives, allowing anyone to reproduce our emulator predictions.

The direct observables that we wish to emulate are the projected galaxy correlation function $w_p(r_p)$ and the excess surface density $\Delta\Sigma(r_p)$. Neglecting sky curvature, residual redshift-space distortion, and higher-order lensing corrections, these are related to the 3D real-space correlation functions by the projection integrals

$$w_p(r_p) = 2 \int_0^{\pi_{\rm max}} \xi_{\rm gg}\left(\sqrt{r^2 + \pi^2}\right) d\pi \,, \tag{10}$$

$$\Delta\Sigma(r_p) = \bar{\rho} \left[\frac{4}{r_p^2} \int_0^{r_p} r \int_0^{\infty} \xi_{\rm gm}\left(\sqrt{r^2 + \pi^2}\right) d\pi dr \right. $$
$$\left. - 2 \int_0^{\infty} \xi_{\rm gm}\left(\sqrt{r_p^2 + \pi^2}\right) d\pi \right] \,, \tag{11}$$

where the cosmic mean matter density is given in comoving coordinates

$$\bar{\rho} = \Omega_m \left(\frac{3 H_0^2}{8\pi G} \right). \tag{12}$$

We report w_p and $\Delta\Sigma$ in units of h^{-1} Mpc and $h\, M_\odot\, {\rm pc}^{-2}$, respectively.

We compute the 3D correlation functions from our emulator via

$$\xi_{\rm gg} = b_g^2 \left(b_{\rm nl}^2 \xi_{\rm mm,\, lin} \right) \,, \tag{13}$$

$$\xi_{\rm gm} = r_{\rm gm} b_g \left(b_{\rm nl}^2 \xi_{\rm mm,\, lin} \right) \,, \tag{14}$$

where all quantities in both equations depend on the 3D separation r.

The choice of the $\pi_{\rm max}$ cutoff for computing $w_p(r_p)$ depends on the redshift survey analysis; ideally one would like $\pi_{\rm max} \to \infty$ to eliminate redshift-space distortions entirely, but estimates of $w_p(r_p)$ can become noisy for very large $\pi_{\rm max}$. In this paper, we choose $\pi_{\rm max} = 100\, h^{-1}$ Mpc. We assume that the impact of residual redshift-space distortion is accounted for in the redshift survey analysis. On the largest scales we consider, the redshift-space correction to w_p may be as large as 15 per cent for our chosen value of $\pi_{\rm max}$ (van den Bosch et al. 2013).

The computation of $\Delta\Sigma$ from GGL observations depends on photometric redshift estimates for the source galaxies and on cosmological parameters used to compute lensing critical surface densities (e.g. Mandelbaum et al. 2005). In a cosmological analysis one might instead use our emulator to predict the more directly observed mean tangential shear

$$\gamma_t(\theta) = \int dz_{\rm lens} \int dz_{\rm src}\, n_{\rm lens}(z_{\rm lens}) n_{\rm src}(z_{\rm src}) \Theta(z_{\rm src} - z_{\rm lens})$$
$$\times \frac{\Delta\Sigma(\theta, z_{\rm lens})}{\Sigma_c(z_{\rm lens}, z_{\rm src})} \,, \tag{15}$$

where the step function $\Theta(x)$ ensures that lensing contributions occur only when $z_{\rm lens} < z_{\rm src}$. Equation 15 can incorporate the cosmological dependence of distance ratios, nuisance parameters for photometric redshift uncertainties, and any signal-to-noise weighting applied to the observations (through additional factors modifying $\Delta\Sigma$). The (comoving) critical surface density Σ_c is

$$\Sigma_c = \frac{c^2}{4\pi G} \frac{D_C(z_{\rm src})}{D_C(z_{\rm lens}) \left[D_C(z_{\rm src}) - D_C(z_{\rm lens}) \right] (1 + z_{\rm lens})} \,, \tag{16}$$

where $D_C(z)$ denotes the comoving distance to redshift z.

For the purpose of the forecasts in this paper, we compute $\gamma_t(r_p)$ predictions from our emulator assuming that $n_{\rm lens}$ is a delta function centered at the effective lens redshift $z_{\rm lens} = 0.27$ (computed for BOSS LOWZ by Singh et al. 2016) and $n_{\rm src}$ is a δ-function centered at an effective source redshift $z_{\rm src} = 0.447$, chosen so that the resulting critical lensing surface density is equal to the value $\Sigma_c = 4.7 \times 10^3\, h\, M_\odot\, {\rm pc}^{-2}$ given by Singh et al. (2016). Using γ_t instead of $\Delta\Sigma$ as the observable in our forecasts introduces an additional dependence on cosmology that significantly modifies the Ω_m-σ_8 degeneracy direction, as the distances entering Σ_c involve an integral over the factor $[\Omega_m(1 + z)^3 + \Omega_\Lambda]^{-1/2}$. We find $d\ln\Sigma_c(z_{\rm lens}, z_{\rm src}; \Omega_m)/d\ln\Omega_m \approx 0.12$ at our fiducial values of Ω_m, $z_{\rm lens}$, and $z_{\rm src}$. Since $\gamma_t \propto \Delta\Sigma\, \Sigma_c^{-1}$, this dependence modifies the best-constrained cosmological parameter by a factor $\approx \Omega_m^{-0.12}$. Because the amplitude of the lensing signal γ_t has an additional dependence on Ω_m beyond that

of $\Delta\Sigma$, using γ_t marginally improves the constraining power of the measurement compared to assuming that $\Delta\Sigma$ is the observable.

Additionally, we correct for the Ω_m-dependence of the projected distance as a function of angular separation and redshift $r_p(\theta, z; \Omega_m)$ by assuming the observer has estimated projected distances in an $\Omega_m = 0.3$ universe. We thus rescale the 'true' distances in which we measure our correlation functions to those our observer would compute when calculating w_p and $\Delta\Sigma$ (eqs. 10 and 11). However, we find that this correction is very small and makes almost no difference to our results.

3 FORECASTING CONSTRAINTS

3.1 Covariance matrices

We use the following expressions from Singh et al. (2016) for the Gaussian component of the observable covariances:

$$\text{cov}_{w_p}(r_i, r_j) = \frac{2A_{ij}}{A_i A_j} \int_0^\infty \frac{k\,dk}{2\pi} J_0(kr_i) J_0(kr_j) \left(b_g^2 P(k) + \frac{1}{n_g} \right)^2 ,$$

$$(17)$$

$$\text{cov}_{\Delta\Sigma}(r_i, r_j) = \frac{V_{ij}}{V_i V_j} \int_0^\infty \frac{k\,dk}{2\pi} J_2(kr_i) J_2(kr_j)$$

$$\times \left[\left(b_g^2 P(k) + \frac{1}{n_g} \right) \left(\Delta\Pi \bar{\rho}^2 P(k) + \frac{\Sigma_c^2 \sigma_\gamma^2}{n_s} \right) + \Delta\Pi \left(\bar{\rho} b_g r_{gm} P(k) \right)^2 \right] .$$

$$(18)$$

These expressions neglect line-of-sight modes, terms that can arise from using a suboptimal estimator that does not subtract the tangential shear around random points, and redshift evolution over the lensed galaxy population. We convert the $\Delta\Sigma$ covariance to our lensing observable γ_t covariance by

$$\text{cov}_{\gamma_t}(r_i, r_j) = \text{cov}_{\Delta\Sigma}(r_i, r_j) \Sigma_c^{-2}. \qquad (19)$$

The area and volume normalization factors in these expressions are:

$$A_{ij} = \int_0^\infty \frac{k\,dk}{2\pi} J_0(kr_i) J_0(kr_j) [W(k)]^2 , \qquad (20)$$

$$A_i = \int_0^\infty \frac{k\,dk}{2\pi} J_0(kr_i) [W(k)]^2 , \qquad (21)$$

$$V_{ij} = L_W A_{ij} , \qquad (22)$$

$$V_i = L_W A_i . \qquad (23)$$

Following Singh et al. (2016), we adopt survey parameters appropriate to BOSS LOWZ galaxy-galaxy lensing. The window function corresponds to a circular survey on the sky of radius $R_s = 1275\,h^{-1}$ Mpc,

$$W(k) = 2\pi R_s^2 \frac{J_1(kR_s)}{kR_s}, \qquad (24)$$

where $n_g = 3 \times 10^{-4}\,h^3$ Mpc^{-3} is the galaxy number density, $\Delta\Pi = 400\,h^{-1}$ Mpc is the effective line-of-sight lensing distance, $L_W = 500\,h^{-1}$ Mpc is the effective line-of-sight survey window, $\Sigma_c = 4.7 \times 10^3\,h\,M_\odot$ pc^{-2} is the critical lensing surface density, $\sigma_\gamma = 0.21$ is the shape noise per galaxy, $n_s = 8\,h^2$ Mpc^{-2} is the effective projected number density of

source galaxies, $\bar{\rho} = \Omega_m (3H_0^2/8\pi G)$ is the cosmic mean matter density (in comoving coordinates), and $P(k)$ is the nonlinear matter power spectrum as computed from our fiducial simulation. At our adopted lens redshift, the survey area is 9000 deg^2 and the nominal source density is 1 arcmin^{-2}. This nominal value is reduced to an effective source density of 0.3 arcmin^{-2} due to redshift cuts (contributing a ~ 50 per cent reduction) and by signal-to-noise weighting (contributing a ~ 30 per cent reduction) (S. Singh, personal communication).

The correlation matrices

$$\text{corr}(r_i, r_j) = \frac{\text{cov}(r_i, r_j)}{\sqrt{\text{cov}(r_i, r_i)\,\text{cov}(r_j, r_j)}} \qquad (25)$$

for our fiducial forecast are shown in Figure 2. The γ_t correlation matrix is nearly diagonal because of the dominant contribution from shot noise, while the w_p correlation matrix has substantial off-diagonal terms for $r_p > 2\,h^{-1}$ Mpc. For purposes of the forecast, we assume that non-Gaussian contributions to the covariance (e.g., Scoccimarro et al. 1999; Cooray & Hu 2001) will be minimized by masking the largest several clusters from the survey in the clustering and GGL measurements used for cosmological analysis. We also assume that the cross-observable covariance (i.e., the covariance between γ_t and w_p) is negligible and the contribution to the covariance from uncertainties in our knowledge of the true cosmic mean observables due to the finite size of our simulations is negligible, although we plan to quantify these contributions to the covariance in future work.[2]

3.2 Model predictions

Figure 3 shows the predicted $w_p(r)$ and $\gamma_t(r)$ from applying our fiducial HOD to our fiducial cosmological simulation (black curve) and to the simulations with higher σ_8 (blue dashed) and higher Ω_m (green dot-dashed). On the scale of this figure, the impact of these parameter changes (6 per cent in σ_8 and 10 per cent in Ω_m) is barely discernible, but one can see that the fractional changes to $\gamma_t(r)$ are larger than the fractional changes to $w_p(r)$. Increasing σ_8 boosts $\xi_{mm}(r)$, but at fixed number density n_{gal} the galaxy bias b_g decreases. For $w_p \propto b_g^2 \xi_{mm}$ the effects nearly cancel, while for $\gamma_t \propto b_g \xi_{mm}$ there is a net increase of amplitude. Increasing Ω_m changes the shape of $\xi_{mm}(r)$ and thus of $w_p(r)$, but the effect of a 10 per cent change is subtle. Increasing Ω_m boosts the amplitude of $\gamma_t(r)$ mainly by increasing the $\bar{\rho}$ prefactor of $\Delta\Sigma$ in equation 11; the change to Σ_c in equation 15 goes in the opposite direction but with much smaller amplitude. The changes of observables are large compared to the statistical errors expected for our fiducial data assumptions, but we have not yet considered degeneracy between cosmological and HOD parameters.

Figure 4 shows derivatives of $\ln w_p(r)$ (left panel) and $\ln \gamma_t(r)$ (right panel) with respect to our eight model parameters. The top panels show derivatives for the conventional HOD parameters: $\ln n_{gal}$, $\ln \sigma_{\log M}$, $\ln M_1/M_{min}$, $\ln \alpha$, and $\Delta\gamma$.

---

[2] The covariance between clustering and galaxy-galaxy lensing has been derived for *angular* separations (Marian et al. 2015), but not, as far as we are aware, in the case of a projected correlation function with $\pi_{max} > 0$.
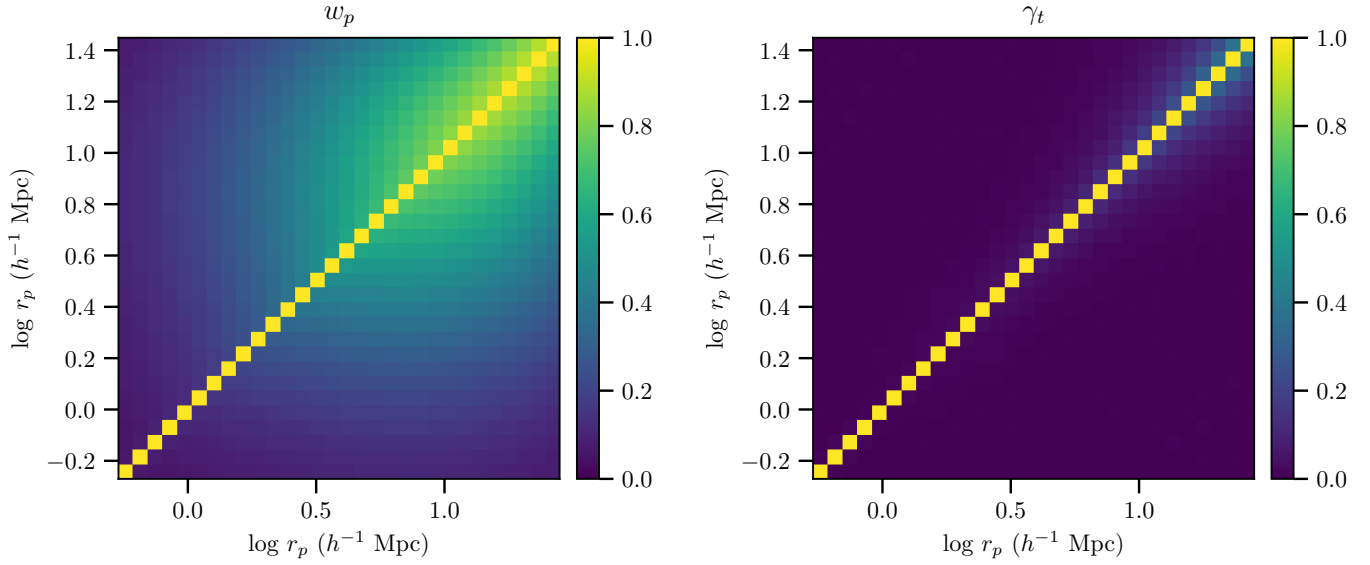
Figure 2. The correlation matrices for our forecast. We compute the covariance matrix for γ_t with the integrals for the Gaussian contributions to the covariance for the variance-minimizing estimator described by Singh et al. (2016). We use similar integrals to compute the covariance for clustering. We assume a source density, area, and redshift properties similar to those of the BOSS LOWZ spectroscopic sample for clustering measurements and SDSS imaging for lensing source galaxies.
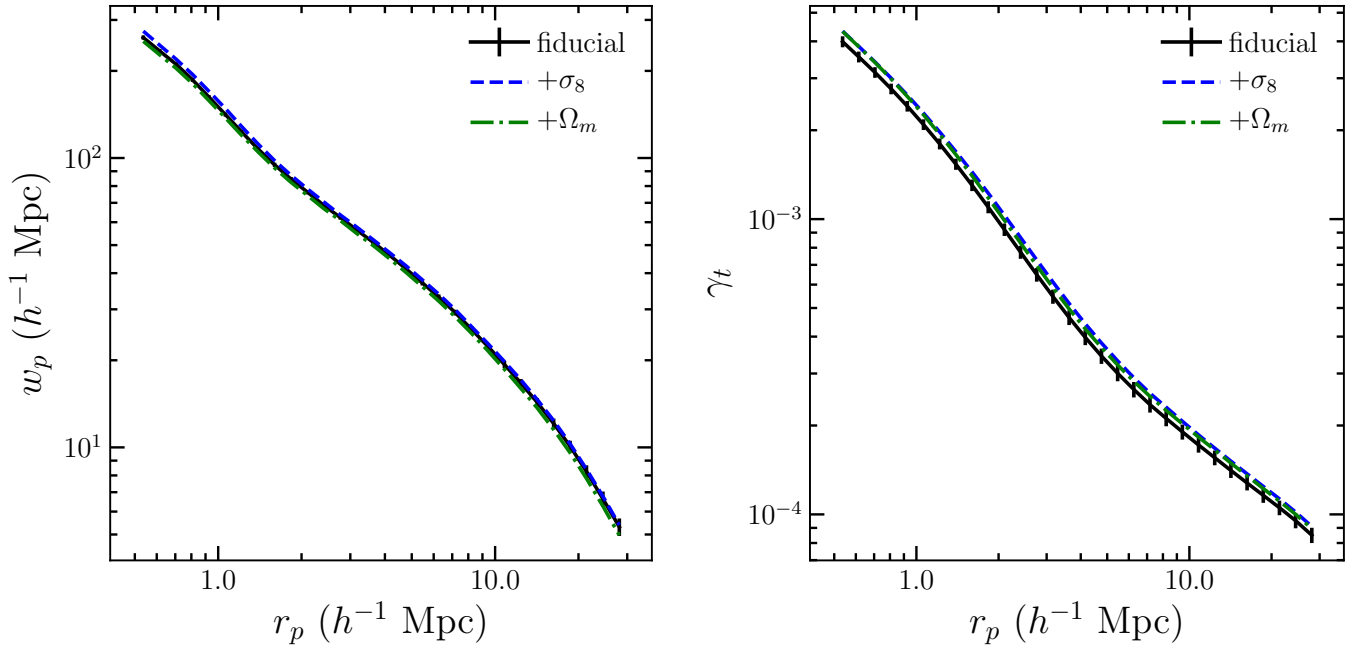

Figure 3. Projected correlation function (left) and tangential shear (right) predicted for our fiducial HOD parameters and the fiducial cosmological simulation (black solid) and for simulations with σ_8 increased by 6 per cent (blue dashed) or Ω_m increased by 10 per cent (green dot-dashed). Error bars on the black curve show the diagonal errors for our assumed data properties, corresponding to BOSS LOWZ lens galaxies and SDSS-depth imaging. The magnitude of changes can be seen more clearly in Figures 4 and 5.

For $w_p(r)$, the large scale behavior is constant in r_p, corresponding to changes in the asymptotic value of b_g, but the derivatives change below $r_p \approx 2\,h^{-1}$ Mpc as the 1-halo contributions to $\xi_{gg}(r)$ become important. Thus, the parameters have degenerate effects on linear scales, but using the full range of $w_p(r)$ can break these degeneracies. Increasing n_{gal} decreases $w_p(r_p)$ on all scales by shifting central galaxies

to less massive, more numerous, less biased halos. Increasing $\sigma_{\log M}$ has a similar effect at large scales, and it suppresses $w_p(r_p)$ more severely in the 1-halo regime because more central galaxies reside in halos that are not massive enough to host satellites. Increasing M_1/M_{min} decreases the overall fraction of satellites, depressing the large scale bias slightly and the 1-halo correlations more severely. Increas-
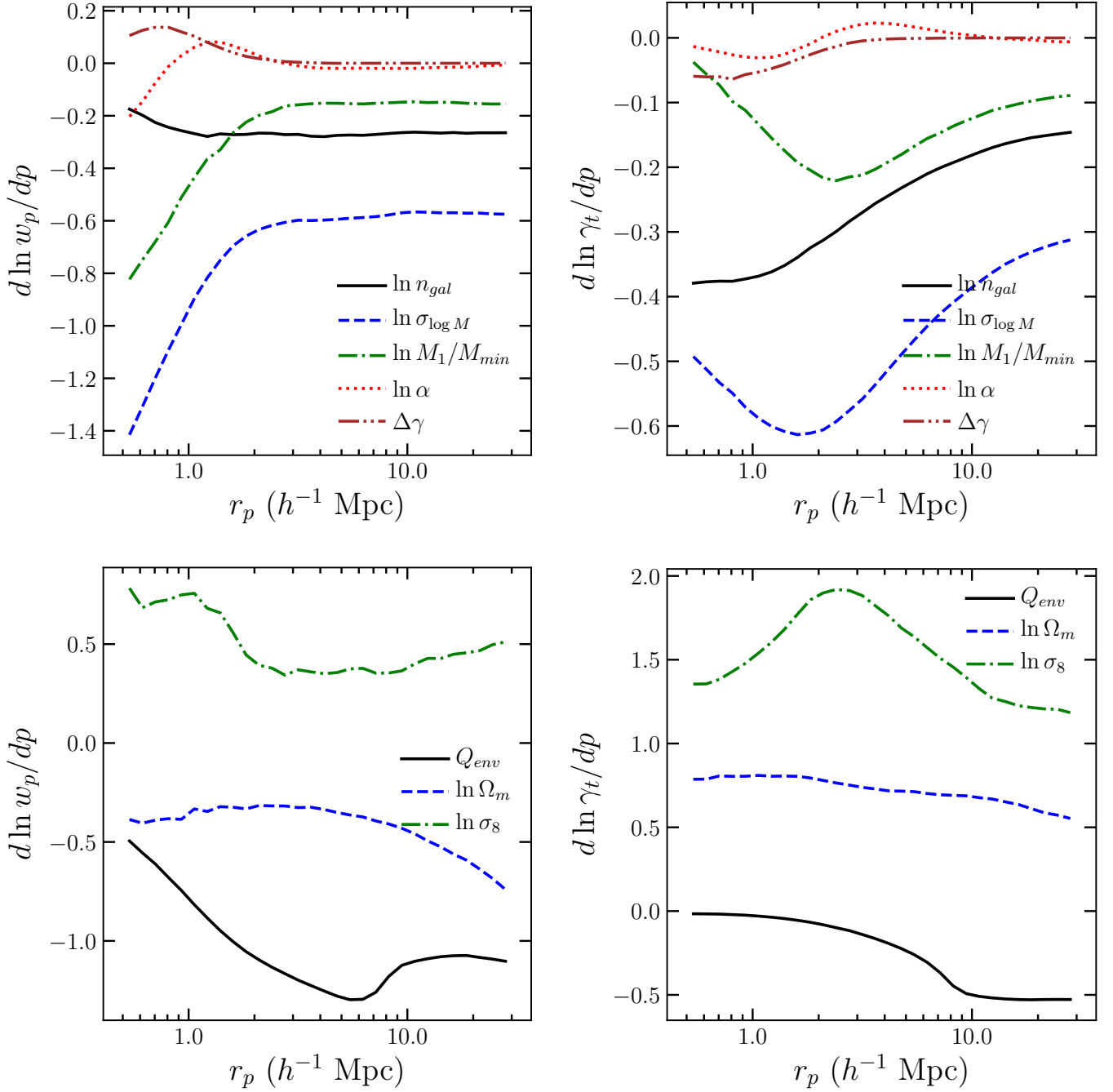
Figure 4. Logarithmic derivatives of w_p (left panels) and γ_t (right panels) with respect to HOD parameters and cosmological parameters, as indicated in the legends. Top panels show derivatives for standard HOD parameters. Bottom panels show derivatives for σ_8, Ω_m, and the environmental HOD parameter Q_{env}.

ing α at fixed M_1/M_{min} has almost no impact at large scales, but it slightly boosts $w_p(r_p)$ on scales corresponding to the virial radii of cluster mass halos, and it depresses $w_p(r_p)$ on small scales where lower mass halos dominate the 1-halo regime. Increasing $\Delta\gamma$ has no impact in the 2-halo regime, and it slightly boosts $w_p(r_p)$ inside $1\,h^{-1}$ Mpc by steepening satellite galaxy profiles.

The influence of these parameters on $\gamma_t(r_p)$ is qualitatively similar, but the scale dependence is more complex because $\Delta\Sigma$ is an *excess* surface density, $\Delta\Sigma(r_p) = \bar{\Sigma}(<$

$r_p) - \bar{\Sigma}(r_p)$ where $\bar{\Sigma}(< r_p)$ is averaged over all radii smaller than r_p (see, e.g. Sheldon et al. 2004). Even at $r_p = 30\,h^{-1}$ Mpc, the impact of n_{gal}, $\sigma_{\log M}$, and M_1/M_{min} has not reached the scale-independence expected asymptotically at large r_p.

The lower panels of Figure 4 show derivatives with respect to the cosmological parameters $\ln\sigma_8$ and $\ln\Omega_m$ and our environment-dependent HOD parameter Q_{env}. Increasing Q_{env} reduces the large scale galaxy bias with other HOD parameters held fixed, because it increases M_{min} (and

thus decreases galaxy numbers) for halos of a given mass in denser environments. The effect of $Q_{\rm env}$ becomes mildly scale-dependent inside the radius $r = 8\,h^{-1}$ Mpc that we are using to define halo environment, and it decreases towards small scales because the 1-halo regime of $\xi_{\rm gg}(r)$ or $\xi_{\rm gm}(r)$ depends only on integrals over the halo mass function and galaxy density profile (see Berlind & Weinberg 2002, eq. 11). For our purposes, the most important effect of $Q_{\rm env}$ is that it decouples the large scale bias from the conventional HOD parameters, so one cannot simply use small and intermediate scale constraints on these parameters to predict the large-scale b_g for a given cosmology.

Increasing σ_8 boosts both w_p and γ_t, but the impact on w_p is smaller because of the cancellation with decreased galaxy bias at fixed $n_{\rm gal}$. Raising σ_8 shifts the inflection of $\xi_{\rm mm}(r)$ at the 1-halo to 2-halo transition outwards, because the virial radii of $M_\star$ halos are slightly larger, which causes the jump in $d\ln w_p/d\ln\sigma_8$ at the transition scale $r_p \approx 1 - 2\,h^{-1}$ Mpc. The corresponding effect in $\gamma_t(r_p)$ is a bump in the derivative at somewhat larger scales.

Increasing Ω_m with fixed $\Omega_m h^2$ makes the matter power spectrum bluer in observable, h^{-1} Mpc units, decreasing w_p at large scales for fixed σ_8.[3] With linear evolution and linear bias, there would be a compensating boost to w_p at small scales, but in our nonlinear calculation w_p is suppressed at all r_p. By contrast, increasing Ω_m boosts $\gamma_t(r_p)$ because of the $\bar\rho$ factor in equation 11, but the logarithmic derivative is below one because of the reduction in $\xi_{\rm mm}(r)$ and the increase of Σ_c in equation 15.

For a more concrete illustration of parameter impacts, Figure 5 shows the fractional changes to $\gamma_t(r_p)$ and $w_p(r_p)$ that arise from changing $M_1/M_{\rm min}$ by ± 0.50 from the fiducial value of 9.55, changing $Q_{\rm env}$ by ± 0.1 from the fiducial value of 0.0, or changing σ_8 by ± 0.05 from the fiducial value of 0.83. Here we have computed $\xi_{\rm gg}(r)$ and $\xi_{\rm gm}(r)$ directly from the populated simulations, but because these correspond to the same finite difference step sizes we use to compute the $b_{\rm nl}$, b_g, and $r_{\rm gm}$ derivatives, the results from using our emulator would be identical.

Changing $M_1/M_{\rm min}$ alters the large scale amplitude of $w_p(r_p)$ and $\gamma_t(r_p)$, and the impact grows at small scales in $w_p(r_p)$ and intermediate scales in $\gamma_t(r_p)$. The effect of $Q_{\rm env}$, by contrast, is largest at large scales, decreasing to nearly zero at sub-Mpc scales in γ_t. Raising or lowering σ_8 raises or lowers the large scale $w_p(r_p)$ and $\gamma_t(r_p)$ as expected, and non-linear evolution induces a distinctive scale-dependence on scales of a few h^{-1} Mpc and below. The fact that each parameter produces a different scale-dependence and has different effects on the two observables demonstrates the potential of precise measurements across the full range of scales to break degeneracies between cosmological quantities and 'nuisance' parameters that describe the relation between galaxies and dark matter.

3.3 Information and Forecasts

Figure 6 shows the parameter constraint forecasts for our fiducial scenario, which adopts the w_p and γ_t covariance

matrices of Figure 2 and a Gaussian prior on $\ln n_{\rm gal}$ with a width of 5 per cent. All of the forecast parameters are in terms of the natural logarithm of the usual parameter, except for parameters that may plausibly be zero or negative (i.e., $Q_{\rm env}$ and $\Delta\gamma$). With analysis down to scales of $0.5\,h^{-1}$ Mpc, a data combination like BOSS LOWZ and SDSS imaging can already yield impressively tight constraints. The best-constrained combination of cosmological parameters is $\sigma_8\Omega_m^p$ with $p = 0.58$, the forecast uncertainty is 1.8 per cent after marginalizing over all HOD parameters. The fully marginalized constraints on σ_8 and Ω_m individually are 4.2 per cent and 6.6 per cent, respectively.

The observational uncertainty in $n_{\rm gal}$ will reflect both cosmic variance and systematic uncertainties in completeness and evolutionary corrections. Here we are treating our galaxy sample as volume-limited and characterized by a single space density, but a full observational analysis might require a redshift-dependent $\bar{n}(z)$. For the individual luminosity-threshold samples of BOSS CMASS galaxies studied by Guo et al. (2014), jackknife error estimates imply $n_{\rm gal}$ uncertainties of about 6 per cent (H. Guo, private communication). We find that the forecast constraint on $n_{\rm gal}$ is essentially equal to our adopted prior (4.9 per cent vs. 5 per cent). Fortunately, varying the $n_{\rm gal}$ prior has negligible impact on the cosmological parameter uncertainties; sharpening the prior to 1 per cent or loosening it to 10 per cent does not change the uncertainties in σ_8, Ω_m, or $\sigma_8\Omega_m^p$ at the two-decimal-place precision quoted in our tables below.

Of other HOD parameters, the most poorly constrained is $\Delta\gamma$, because its largest effects are limited to scales below the smallest r_p we consider. For the same reason, uncertainties in $\Delta\gamma$ have little impact on the uncertainties in cosmological or other HOD parameters. Uncertainties in $\sigma_{\log M}$, $M_1/M_{\rm min}$, and α are 9 per cent, 19 per cent and 11 per cent, respectively. Interestingly, the assembly bias parameter $Q_{\rm env}$ is quite tightly constrained, with a forecast uncertainty of 0.028 dex. Changing the $n_{\rm gal}$ prior to 10 per cent (1 per cent) moderately loosens (tightens) the constraints on $\sigma_{\log M}$ and $M_1/M_{\rm min}$ but has negligible effect on other parameters.

Tables 1 and 2 compare forecasts for a variety of other scenarios, with Table 1 listing the marginalized constraints on σ_8, Ω_m, and individual HOD parameters and Table 2 listing the best constrained parameter combination of the form $\sigma_8\Omega_m^p$. We first consider the impact of increasing the effective weak lensing source density by a factor of 10 to 3 galaxies arcmin^{-2}, comparable to the source density in the Dark Energy Survey instead of SDSS imaging. This change lowers the shape noise contribution to the γ_t covariance matrix (eq. 18). The precision of $\sigma_8\Omega_m^p$ improves by a factor of two, to 0.9 per cent. The individual constraints on σ_8 and Ω_m improve by a factor ≈ 1.5.

Returning to the fiducial source density of 1 arcmin^{-2}, we next consider the impact of eliminating the γ_t measurements at $r_p < 5\,h^{-1}$ Mpc. The constraint on $\sigma_8\Omega_m^p$ degrades to 2.2 per cent; the value of p in the best constrained combination depends on the data being considered, increasing slightly to $p = 0.65$ in this case. Degradation can arise from the loss of aggregate statistical precision in the $\gamma_t(r_p)$ measurement – with fewer points, the overall amplitude is less well determined and from the loss of leverage on parameter degeneracies for the reduced range of scales. To isolate the

---

[3] The power spectrum shape parameter $\Gamma = \Omega_m h$ increases, shifting the turnover in $P(k)$ to higher k in h Mpc^{-1} units.
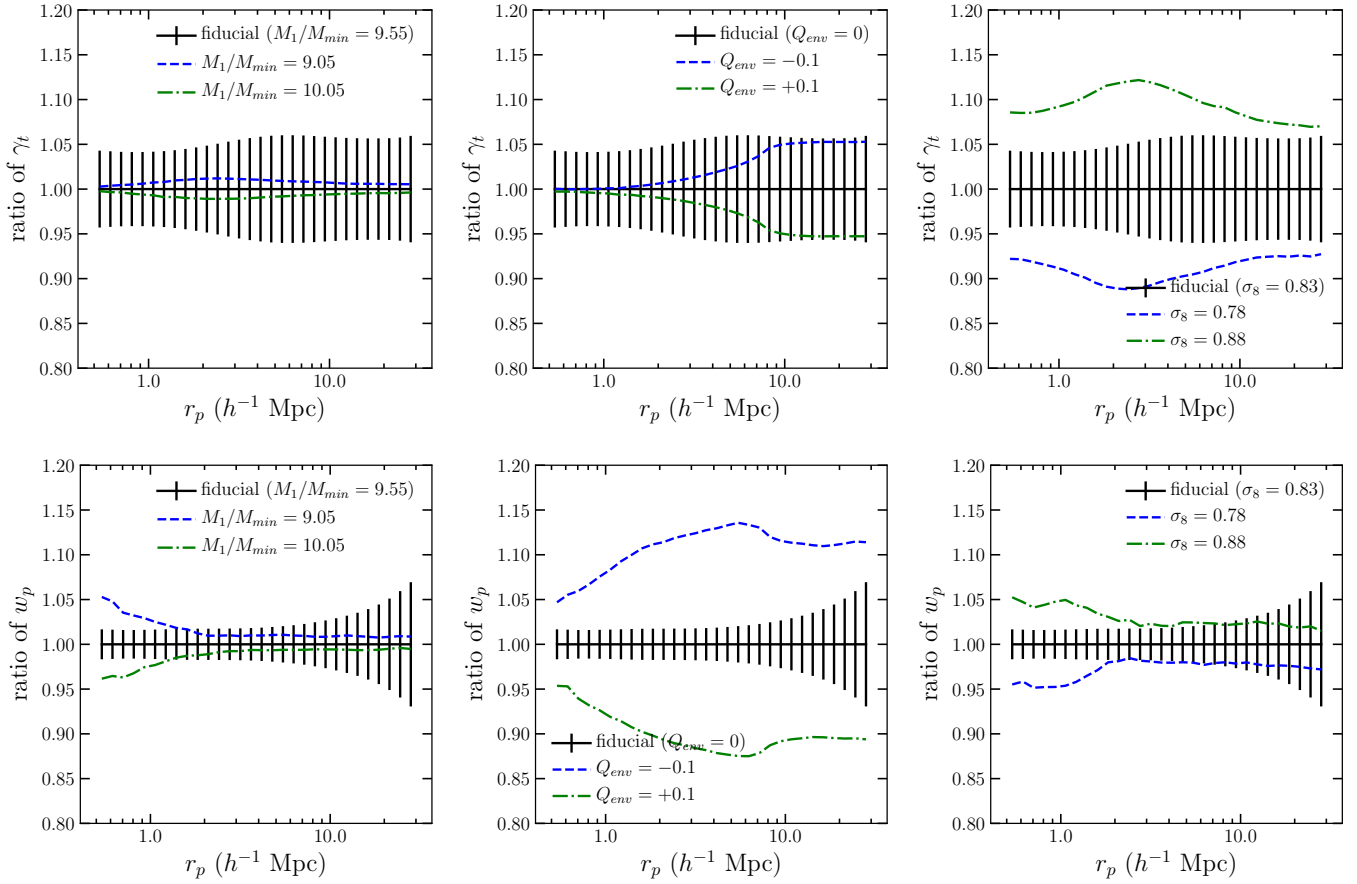
Figure 5. The ratios of observables for changes in some parameters. The leftmost panel shows the effect of the HOD parameter $M_1/M_{\min}$ on the observables w_p and γ_t. The middle panel shows the effect of the environmental density parameter Q_{env}, and the rightmost panel shows the effect of σ_8. The error bars are the same as those shown in Figure 3.

second effect, we rescale the $\gamma_t(r_p)$ covariance matrix C_{ij} by a constant factor that restores the signal-to-noise ratio $(S/N) = \left[D^T C^{-1} D \right]^{1/2}$ to its value in the fiducial forecast, where D is the data vector. With this rescaling, the constraint on $\sigma_8 \Omega_m^p$ *improves* relative to the fiducial forecast, from 1.8 per cent to 1.2 per cent. Of course, one is not able to make this adjustment in a real observational situation; the weak lensing error bars at large scales do not decrease because one chooses to ignore small scales in the modeling. However, this experiment shows that the 'per unit' information content of the large-scale $\gamma_t(r_p)$ measurements is more significant than the small scale measurements because they suffer less degeneracy with galaxy bias parameters. The error bars on some HOD parameters, particularly $\sigma_{\log M}$, $M_1/M_{\min}$, and Q_{env}, do get worse when eliminating small scale $\gamma_t(r_p)$ and rescaling the covariance matrix.

For $w_p(r_p)$, the situation is reversed. Excluding points with $r_p < 5\,h^{-1}$ Mpc degrades the precision on $\sigma_8 \Omega_m^p$ by more than a factor of two, from 1.8 per cent to 4.0 per cent, and rescaling to restore the signal-to-noise ratio of the fiducial measurement only improves the precision to 2.4 per cent. Without rescaling, the constraints on HOD parameters become dramatically worse, especially for the parameters α and $\Delta\gamma$ whose largest impact is on small scales. With rescaling, the constraints on $\sigma_{\log M}$, $M_1/M_{\min}$, and Q_{env} are actu-

ally better than in the fiducial case, but the errors on α and $\Delta\gamma$ remain large, and the degeneracy with $\sigma_8 \Omega_m^p$ is evidently large enough to degrade its precision. The marginalized error on Ω_m itself improves by nearly a factor of three over the fiducial case because of the better measurement of the large scale shape of $w_p(r_p)$, and the marginalized constraint on σ_8 improves moderately as a result. Overall, this experiment shows that the information from nonlinear scales of $w_p(r_p)$ improves the cosmological constraining power of clustering and GGL by breaking degeneracies with HOD parameters that describe the relation between galaxies and dark matter. We caution that our Taylor expansion and Fisher matrix calculation may become inaccurate with large uncertainties in α and $\Delta\gamma$, but this inaccuracy will not affect our qualitative conclusions.

Finally, we consider the specific cuts adopted by Mandelbaum et al. (2013), excluding $r_p < 2\,h^{-1}$ Mpc for $\gamma_t(r_p)$ and $r_p < 4\,h^{-1}$ Mpc for $w_p(r_p)$. These cuts increase the error on $\sigma_8 \Omega_m^p$ by more than a factor of two, from 1.8 per cent to 3.8 per cent. The individual marginalized constraints on σ_8 and Ω_m grow by slightly more and slightly less than a factor of two, respectively. We conclude that the gains in cosmological precision achievable from our more comprehensive theoretical modeling, relative to the more conservative approach of Mandelbaum et al. (2013), are about a factor of

two in parameter errors, equivalent to the effect of a fourfold increase in survey area.

Figure 7 provides further insight into the degeneracy of cosmological and HOD parameters and the role of $w_p(r_p)$ and $\gamma_t(r_p)$ in breaking them. The leftmost points on each sequence show the fractional uncertainty in σ_8 if all HOD parameters and Ω_m are held fixed to their true values. Our fiducial data combination could measure σ_8 to 0.56 per cent if all other parameters were known perfectly. We then unleash the HOD parameters in sequence, adding successively more degrees of freedom to the HOD model. At each step in the sequence, we choose the parameter that produces the sharpest increase of the σ_8 uncertainty when it is set free, for the fiducial data case. Ordered this way, the parameter with the highest leverage is $n_{\rm gal}$, because with other HOD parameters fixed a 5 per cent uncertainty in $n_{\rm gal}$ (set by our prior) can change the galaxy bias factor significantly. We previously found that varying the $n_{\rm gal}$ prior from 0.01 to 0.10 had negligible impact on cosmological precision (see Tables 1 and 2), but that was with other HOD parameters free to compensate for its effect. Adding more HOD parameters steadily increases the marginalized σ_8 error, reaching 1.8 per cent with the full parameter set. Because of the usual cosmological degeneracy between σ_8 and Ω_m, the marginalized σ_8 error rises to 4.2 per cent when Ω_m is also free. However, the fractional error on σ_8 with fixed Ω_m is the same as the fractional error on the best constrained $\sigma_8\Omega_m^p$ combination, and we view this as the best characterization of the statistical power of a combined clustering + GGL data set.

When small scales of $\gamma_t(r_p)$ are dropped (green curve in Figure 7), the precision on σ_8 as the sole free parameter degrades by a factor of 1.5, from 0.56 per cent to 0.83 per cent. However, the uncertainty associated with scale-dependent galaxy bias is reduced when the small scale $\gamma_t(r_p)$ are not considered, so the degradation with all HOD parameters free is only a factor of 1.2 (2.2 per cent versus 1.8 per cent, as listed in Table 2).

Dropping the small scale $w_p(r_p)$ data instead (red curve) produces minimal degradation when HOD parameters are fixed, but now these parameters are poorly constrained and thus have a large impact once they are set free. In particular, the assembly bias parameter $Q_{\rm env}$ has a much larger uncertainty in this case (see Table 1) and has a more pronounced impact on cosmological parameter uncertainty. Raising the weak lensing source density (blue curve) improves the σ_8 precision at fixed HOD by a factor of 2.5 (0.22 per cent versus 0.56 per cent), nearly the full factor of $10^{1/3} = 3.16$ that would be expected if weak lensing shape noise were the only effect limiting the measurement precision. The relative impact of galaxy bias uncertainties is larger when the weak lensing precision is higher, but not drastically so; when all HOD parameters are free, the σ_8 precision is still a factor of two better than that of the fiducial case (0.9 per cent versus 1.8 per cent).

The final lines of Tables 1 and 2 show forecasts based on the $w_p(r_p)$ data alone, with no GGL information. In a pure linear theory calculation with galaxy bias b_g as a free parameter, the shape of $w_p(r_p)$ would constrain Ω_m, but there would be no constraint on σ_8 because it would be fully degenerate with b_g. Our non-linear forecast with an HOD description of galaxy bias yields an 11 per cent constraint

on $\sigma_8\Omega_m^p$ and a 12 per cent marginalized constraint on σ_8. These are much worse than the 1.8 per cent and 4.2 per cent fiducial forecasts, demonstrating that the great majority of the cosmological information is coming from the *combination* of clustering and GGL, not from the high precision clustering measurements on their own. The uncertainty in $Q_{\rm env}$ is also substantially larger for the clustering only case (0.058 vs. 0.028). This difference shows that, while some of the information about $Q_{\rm env}$ is coming from the distinctive scale dependence that it produces, much of it coming from the relative strength of clustering and GGL. This suggests that the clustering + GGL combination could be a useful diagnostic of galaxy assembly bias, especially if one has strong external constraints on Ω_m. Physically, assembly bias is the main effect that can alter the large scale galaxy bias given constraints on other HOD parameters from small and intermediate scales. The clustering + GGL combination breaks the degeneracy of b_g and σ_8, even on linear scales, so it can test for the presence or absence of this effect.

We also include a forecast for a hypothetical scenario in which we can correctly label all observed galaxies as central galaxies or satellite galaxies and then only use the central galaxies to compute the observed correlation functions and number densities ('centrals only'). Some analytic forecasts (e.g., Yoo & Seljak 2012) and cosmological analyses of galaxy-galaxy lensing implicitly assume all observed galaxies are centrals, but in our analysis framework we can marginalize over the satellite galaxy properties as well. This forecast shows that the cosmological constraints are not degraded by using only the information contained in the statistics of central galaxies, and that, in principle, regardless of the complexity of the physics of satellite galaxies, significant cosmological information exists at the small scales considered in this work. This conclusion should also apply in the presence of incompleteness of the galaxy sample or miscentering of galaxies. For the fiducial forecast scenario with all observed galaxies (both centrals and satellites), we have explicitly checked that adding a completeness fraction parameter $f_{\rm cen}$ to central galaxies does not degrade our cosmological parameter constraints. The effect of central incompleteness, to a first approximation, mimicks the effects of miscentering of central galaxies with respect to the halo center, and thus serves as a sufficient test that our cosmological constraints are relatively robust to incompleteness or miscentering of galaxies. Additionally, for the fiducial forecast scenario, we have explicitly checked that marginalizing over all of the parameters of our adopted concentration-mass relation (as used to determine the satellite galaxy profile) does not affect our cosmological constraints to three decimal places. This is because the overall amplitude of the concentration of halos, the power-law slope of the relation, and the cubic term (parameterized by γ in eq. 1) are all almost degenerate with a change in power-law slope of the NFW profile (parameterized by $\Delta\gamma$) for the scales we consider. (This can be seen by comparing the 'marginalizing over concentration-mass relation' forecast in Tables 1 and 2 to the fiducial forecast.)

Excising scales below $8\,h^{-1}$ Mpc, we have checked that the 'centrals only' forecasts yield cosmological parameter uncertainties a factor ~ 2 *smaller* than equivalent forecasts for the full galaxy population that marginalize over satellite

galaxy properties and consider the same scales. This suggests that marginalizing over the properties of the satellite galaxy population, even for samples with low satellite fractions such as LOWZ, may be important in correctly estimating the uncertainties on cosmological parameters in a galaxy-galaxy lensing analysis, especially when using a GGL estimator that always contains contributions from small scales such as γ_t (see Appendix A for a comparison of the scale-dependence of GGL estimators).

As a preliminary test of our emulator accuracy, we have drawn 20 samples from the posterior of the fiducial forecast while fixing cosmological parameters to those of the fiducial cosmology. Computing the galaxy populations and correlation functions numerically, we compare to the predictions of w_p from our emulator, finding that on scales greater than $2\,h^{-1}$ Mpc, the standard deviation of emulator accuracy is substantially less than the diagonal error bars derived from our covariance matrices. Within $2\,h^{-1}$ Mpc, however, we find that the dispersion in emulator accuracy is comparable to the size of the diagonal error bars on our fiducial projected clustering signal. With respect to the lensing signal however, we find that the emulator inaccuracy is very subdominant compared to the error bars on γ_t on all scales that we use for forecasts. For applications of our emulator framework to cosmological analyses, we therefore suggest that second-order derivatives be used for emulating w_p as a function of HOD parameters and that the emulator should be re-centered about the best-fit parameters as part of the fitting procedure, which should converge in a small number of iterations. We leave investigation of emulator accuracy with respect to the cosmological parameters to future work.

4 DISCUSSION AND CONCLUSIONS

Several observational studies have demonstrated the promise of combining galaxy clustering and GGL to constrain cosmological parameters and test ΛCDM+GR predictions of matter clustering (Mandelbaum et al. 2013; More et al. 2015; Hildebrandt et al. 2017; Leauthaud et al. 2017; DES Collaboration et al. 2017). Building on earlier theoretical studies by Yoo et al. (2006), Leauthaud et al. (2011), Cacciato et al. (2012), and Yoo & Seljak (2012), our investigation demonstrates the power of extending these analyses down to small scales using a flexible model for the relation between galaxies and dark matter. As a fiducial case, we consider HOD parameters and covariance matrices scaled to the BOSS LOWZ galaxy lens sample and SDSS-depth imaging (approximately one source galaxy per arcmin^2) over 9,000 deg^2 (Singh et al. 2016) for weak lensing measurements. Extending the analysis of $\gamma_t(r_p)$ and $w_p(r_p)$ to $0.5\,h^{-1}$ Mpc improves the precision of the best-constrained $\sigma_8\Omega_m^p$ combination by more than a factor of two (1.8% vs. 3.8%) relative to the more conservative cuts ($2\,h^{-1}$ Mpc for γ_t and $4\,h^{-1}$ Mpc for w_p) adopted by Mandelbaum et al. (2013) for their analysis of SDSS DR7, which uses the perturbative bias model of Baldauf et al. (2010). Some of the gain in parameter precision comes directly from using the small scale $\gamma_t(r_p)$ measurements, which provide additional leverage on the amplitude of the galaxy-matter cross-correlation. However, the largest gains come from using the smaller scales of

$w_p(r_p)$ to constrain HOD parameters, which allows our model to make better use of the large scale $\gamma_t(r_p)$ data for the cosmological constraints.

The emulator approach described in §2 makes a fully non-linear, N-body + HOD approach practical for statistical analysis. In this paper we have considered only σ_8 and Ω_m as the varying cosmological parameters, and we have computed results at $z = 0.3$. However, because we construct our emulator to compute ratios of correlation functions starting from $\xi_{\rm mm,lin}$, it can accommodate some range of cosmological parameters. We will improve the emulator in future work using a grid of cosmological simulations, which will also allow leave-one-out tests for the emulator's accuracy and more systematic study of its range of validity. Detailed predictions for an observational data set also require information about the redshift distributions of the lens and source samples and may include nuisance parameters that describe observational or theoretical systematics. Rather than incorporate these survey-specific elements into our emulator, we focus on predicting the two quantities, $\xi_{\rm gg}$ and $\xi_{\rm gm}$, that require non-linear clustering calculations.

The main limitation of the emulator approach as pursued here is the need to retune the fiducial HOD for each galaxy lens sample, and to model the range of redshifts probed by that sample. This does not require new simulations, but it does require new HOD populations and correlation function measurements for each lens sample being considered.

A novel aspect of our model is inclusion of a parameterized description of HOD environmental variation, to capture the potential effects of galaxy assembly bias. This prescription allows the large scale galaxy bias to be at least partly decoupled from the "classic" HOD parameters constrained by small and intermediate scale clustering. It is encouraging that this new degree of freedom in the galaxy bias model does not lead to substantial degradation of the cosmological parameter constraints. Indeed, we find that the combination of clustering and GGL gives interestingly tight constraints on $Q_{\rm env}$ even with free cosmological parameters. To date, most observational tests for galaxy assembly bias have focused on comparing clustering of subsets of the red galaxies. The approach outlined here could provide a way to test for assembly bias in luminosity- or mass-selected galaxy samples. Our $Q_{\rm env}$ parameterization predicts a scale-dependence of galaxy bias that might be different from that predicted by a specific physical model that ties galaxy properties to halo assembly. The best way to test the adequacy of our model is to apply it to galaxy populations drawn from hydrodynamic simulations or to simulations that populate N-body halos using abundance and age-matching prescriptions (e.g., Hearin & Watson 2013; Lehmann et al. 2017) or semi-analytic galaxy formation models. Hydrodynamic simulations are also needed to test for baryonic effects on the mass distribution, including the impact of subhalos around satellite galaxies. Yoo et al. (2006) found little impact of subhalos on GGL, but their hydrodynamic simulations were too small for tests at the level of precision needed for current data sets. More recently, galaxy-galaxy lensing was considered by van Daalen et al. (2014) in the context of comparing hydrodynamic simulations with and without a given form of strong AGN feedback, who found virtually no impact on GGL on scales larger than approximately twice the halo
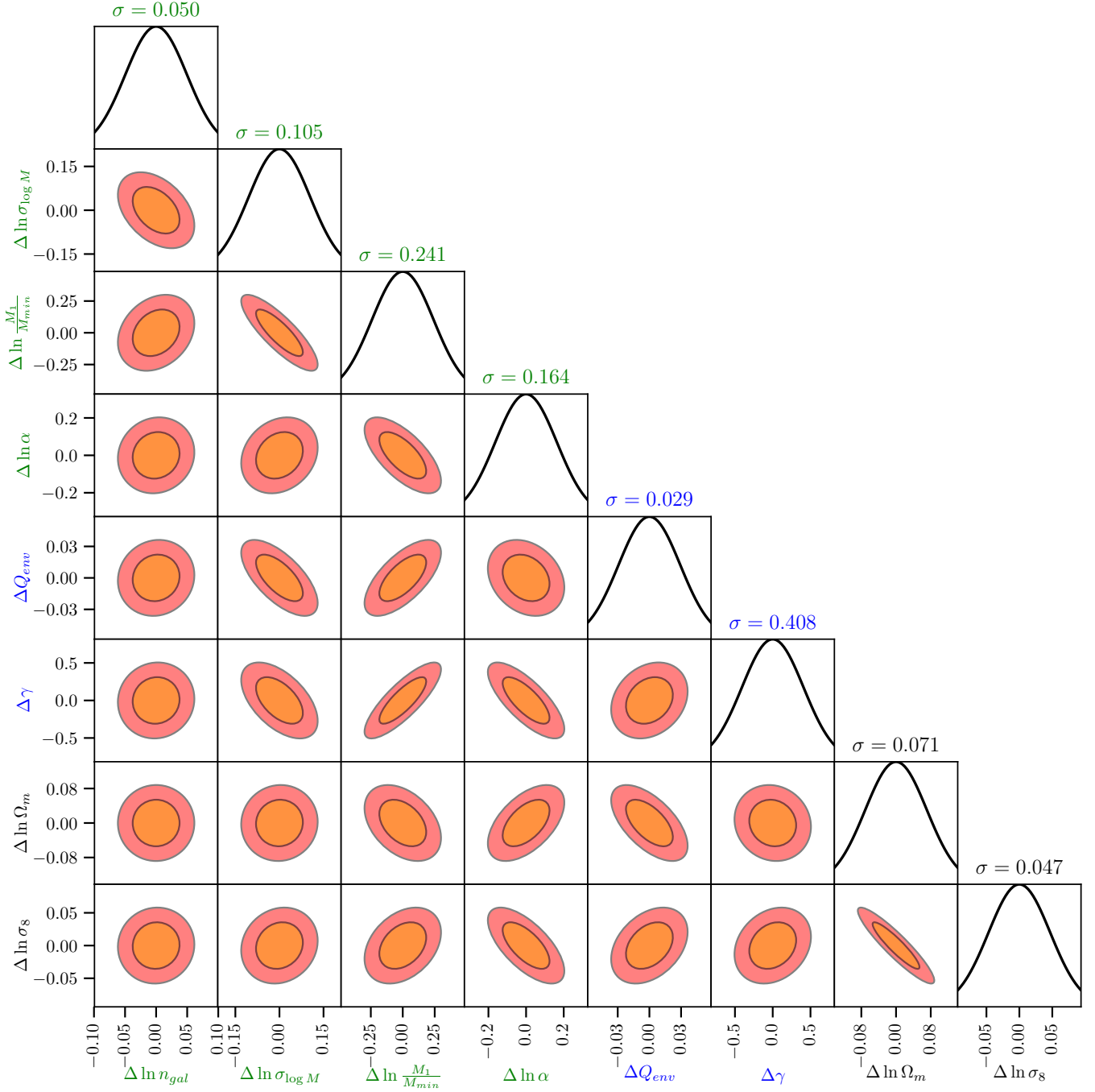
Figure 6. The fiducial forecast. We use the predicted projected galaxy correlation w_p and the mean tangential shear γ_t on scales $0.5 < r_p < 30\ h^{-1}$ Mpc. Tight cosmological constraints are possible (4.2% on σ_8, 6.6% on Ω_m) even after marginalizing over assembly bias and HOD parameters.

virial radius (when modeling galaxy samples as a function of number density rather than at fixed halo mass) but ~ 10 per cent effects on smaller scales due to scale-dependent effects on ξ_{gm}, with substantially smaller effects on the scale-dependence of ξ_{gg}. Since the improved constraining power by using small scales in our forecasts is primarily due to the small-scale clustering rather than small-scale lensing, our results may be relatively insensitive to baryonic effects on the matter distribution, but more work is needed to

assess any potential bias in cosmological parameters due to baryonic effects in our analysis framework.

The stakes for precise and accurate joint clustering and GGL analyses are high, because many cosmic shear and GGL analyses to date yield estimates of $\sigma_8 \Omega_m^{0.5}$ that are lower than that predicted by a Planck-normalized ΛCDM model (e.g. Heymans et al. 2012; Hildebrandt et al. 2017; DES Collaboration et al. 2017). The statistical significance for any one data set is usually $\lesssim 2\sigma$. Improving lensing

Table 1. Forecasts of fractional uncertainties in cosmological and HOD parameters for various scenarios. For some scenarios, we show the forecast where the signal-to-noise is rescaled to match the signal-to-noise of the fiducial forecast (indicated by "rescaled S/N").

	$\Delta \ln n_{\rm gal}$	$\Delta \ln \sigma_{\log M}$	$\Delta \ln \frac{M_1}{M_{\min}}$	$\Delta \ln \alpha$	$\Delta Q_{\rm env}$	$\Delta \gamma$	$\Delta \ln \Omega_m$	$\Delta \ln \sigma_8$
fiducial	0.050	0.105	0.241	0.164	0.029	0.408	0.071	0.047
10x source density	0.049	0.067	0.194	0.148	0.018	0.343	0.049	0.032
excluding $\gamma_t < 5\,h^{-1}$ Mpc	0.050	0.236	0.379	0.171	0.061	0.423	0.080	0.060
excluding $\gamma_t < 5\,h^{-1}$ Mpc (rescaled S/N)	0.050	0.218	0.357	0.167	0.053	0.420	0.076	0.057
excluding $w_p < 5\,h^{-1}$ Mpc	0.050	0.419	0.762	1.288	0.092	2.546	0.105	0.101
excluding $w_p < 5\,h^{-1}$ Mpc (rescaled S/N)	0.050	0.233	0.496	1.001	0.046	1.279	0.045	0.057
excluding both $< 5\,h^{-1}$ Mpc	0.050	1.694	4.866	5.282	0.120	33.739	0.137	0.125
excluding $< 2\ (\gamma_t)$ and $< 4\ (w_p)\ h^{-1}$ Mpc	0.050	0.693	2.145	3.087	0.087	4.932	0.095	0.088
excluding $< 12\ (\gamma_t)$ and $< 8\ (w_p)\ h^{-1}$ Mpc	0.050	2.053	5.855	6.146	0.362	45.710	0.162	0.178
$\Delta \ln n_{\rm gal} = 0.01$	0.010	0.096	0.234	0.163	0.029	0.408	0.071	0.047
$\Delta \ln n_{\rm gal} = 0.1$	0.097	0.127	0.262	0.165	0.029	0.409	0.071	0.047
no lensing	0.050	0.257	0.452	0.234	0.067	0.454	0.120	0.110
$r_{\min} = 0.1\,h^{-1}$ Mpc	0.048	0.061	0.089	0.107	0.020	0.056	0.058	0.040
centrals only	0.043	0.020	—	—	0.023	—	0.070	0.044
including M_0/M_1 as a free parameter	0.050	0.115	0.430	0.234	0.031	0.570	0.072	0.049
marginalizing over concentration-mass relation	0.050	0.107	0.247	0.302	0.030	2.218	0.072	0.047

Table 2. Best-constrained parameters for forecasts.

	p	best-constrained $\sigma_8 \Omega_m^p$
fiducial	0.605	0.019
10x source density	0.618	0.009
excluding $\gamma_t < 5\,h^{-1}$ Mpc	0.690	0.023
excluding $\gamma_t < 5\,h^{-1}$ Mpc (rescaled S/N)	0.726	0.015
excluding $w_p < 5\,h^{-1}$ Mpc	0.882	0.040
excluding $w_p < 5\,h^{-1}$ Mpc (rescaled S/N)	0.988	0.036
excluding both $< 5\,h^{-1}$ Mpc	0.845	0.049
excluding $< 2\ (\gamma_t)$ and $< 4\ (w_p)\ h^{-1}$ Mpc	0.828	0.041
excluding $< 12\ (\gamma_t)$ and $< 8\ (w_p)\ h^{-1}$ Mpc	0.990	0.077
$\Delta \ln n_{\rm gal} = 0.01$	0.605	0.018
$\Delta \ln n_{\rm gal} = 0.1$	0.605	0.019
no lensing	-0.255	0.105
$r_{\min} = 0.1\,h^{-1}$ Mpc	0.658	0.014
centrals only	0.589	0.014
including M_0/M_1 as a free parameter	0.622	0.020
marginalizing over concentration-mass relation	0.603	0.019

and CMB analyses could remove this tension, or they could sharpen it into strong evidence for new physics. The largest magnitude of discrepancy is found by Leauthaud et al. (2017), who measure GGL for BOSS CMASS galaxies from $250\ \deg^2$ of deep imaging data and compare their measurements to predictions from a variety of mock catalogs that are designed to reproduce observed CMASS galaxy clustering. On scales of $0.3 - 3\,h^{-1}$ Mpc the discrepancy in $\gamma_t(r_p)$ is about 20% and well outside the statistical errors, and on scales of $0.1 - 0.3\,h^{-1}$ Mpc it is larger still. (However, we caution that the authors did not consider the possible effects of an incompleteness of the galaxy sample that is unexpectedly large or with a complicated halo mass dependence, or of miscentering of central galaxies with respect to the halo center, see e.g., More et al. 2015). The results of McEwen & Weinberg (2016) suggest that this discrepancy should be robust to uncertainties about galaxy assembly bias, because they find that even when strong assembly bias is present, an HOD model that reproduces the observed galaxy clustering also predicts the correct ratio $\xi_{\rm gm}(r)/\xi_{\rm gg}(r)$. Our results here provide further support for

this view, showing that clustering and GGL can yield strong cosmological constraints even when marginalizing over our parameterized assembly bias prescription.

For our fiducial data assumptions, we forecast a 1.8% error on $\sigma_8 \Omega_m^{0.58}$. For comparison, the error on $S_8 \equiv \sigma_8 (\Omega_m/0.3)^{0.5}$ from DES Year 1 data is 2.9% (DES Collaboration et al. 2017). This constraint uses clustering (Elvin-Poole et al. 2017) and GGL (Prat et al. 2017) of the DES "redMaGiC" galaxy sample (Elvin-Poole et al. 2017; Rozo et al. 2016) *and* cosmic shear from the same imaging data (Troxel et al. 2017), comprising 26 million galaxy shape measurements over 1321 $\deg^2$ (5.4 gal/arcmin^2). The DES analysis includes marginalization over several systematics not considered here, such as shear calibration uncertainties, photometric redshift biases, and galaxy intrinsic alignments. These uncertainties must be accounted for in any GGL analysis, and they will degrade the precision of cosmological measurements below that of our forecasts. Nonetheless, our results show that extending to non-linear scales allows even SDSS-depth imaging to achieve constraints competitive with the best current weak lensing data sets.
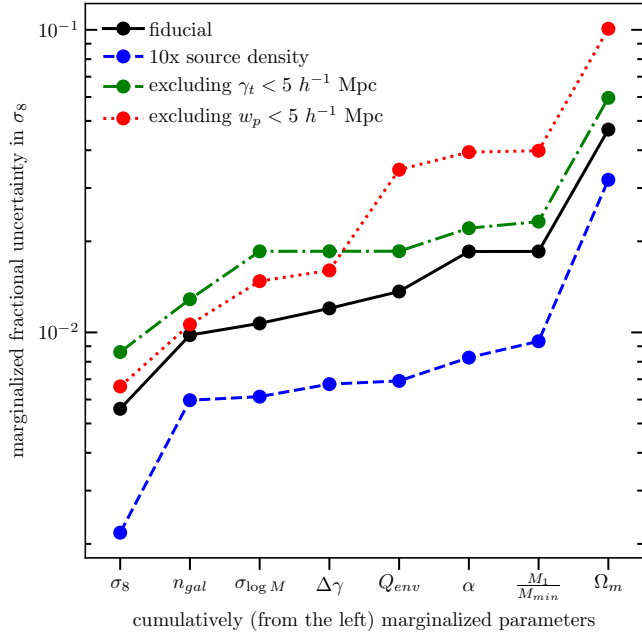
Figure 7. A comparison of forecasts on marginalized σ_8 for various scenarios. We show the marginalized fractional uncertainty on σ_8 as we marginalize over an increasing number of parameters from left-to-right. The order of parameters is set such that Ω_m is chosen to be the last-marginalized parameter, σ_8 is chosen to be the first parameter, and the other parameters are ordered such that the steepest rise in fractional uncertainty is obtained for the fiducial forecast scenario.

Our emulator results (detailed in Appendix B) can be applied as they are to GGL measurements of the BOSS LOWZ sample (keeping in mind the caveats about emulator accuracy that we detail in section 3.3). For imaging data significantly deeper than SDSS, better constraints will come from higher redshift lens populations that probe larger volumes, such as the BOSS CMASS spectroscopic sample or photometrically defined samples such as DES redMaGiC. We will investigate predictions for such samples in future work. There are many considerations that go into choosing a lens sample, including lens density and redshift distribution, overlap with deep imaging data for spectroscopic samples, accuracy of photometric redshifts for photometric samples, and observational uncertainties such as incompleteness, contamination, or depth variations. Our results suggest that physical simplicity should be an additional consideration in defining lens samples, since the extension of analyses to non-linear scales can substantially improve their constraining power but requires accurate modeling. Data sets emerging over the next few years should enable tests of the matter clustering predicted by General Relativity at the percent or even sub-percent level, with the potential to reveal profound new physics or to provide powerful confirmation of the reigning theories of dark energy and cosmological gravity.

REFERENCES

Abazajian K. N., et al., 2009, ApJS, 182, 543
Aihara H., et al., 2017, preprint, (arXiv:1704.05858)
Baldauf T., Smith R. E., Seljak U., Mandelbaum R., 2010, Phys. Rev. D, 81, 063531
Behroozi P. S., Wechsler R. H., Wu H.-Y., 2013, ApJ, 762, 109
Benson A. J., Cole S., Frenk C. S., Baugh C. M., Lacey C. G., 2000, MNRAS, 311, 793
Berlind A. A., Weinberg D. H., 2002, ApJ, 575, 587
Bond J. R., Cole S., Efstathiou G., Kaiser N., 1991, ApJ, 379, 440
Bryan G. L., Norman M. L., 1998, ApJ, 495, 80
Cacciato M., van den Bosch F. C., More S., Li R., Mo H. J., Yang X., 2009, MNRAS, 394, 929
Cacciato M., Lahav O., van den Bosch F. C., Hoekstra H., Dekel A., 2012, MNRAS, 426, 566
Cacciato M., van den Bosch F. C., More S., Mo H., Yang X., 2013, MNRAS, 430, 767
Center O. S., 1987, Ohio Supercomputer Center, http://osc.edu/ark:/19495/f5s1ph73
Cooray A., Hu W., 2001, ApJ, 554, 56
Correa C. A., Wyithe J. S. B., Schaye J., Duffy A. R., 2015, MNRAS, 452, 1217
Coupon J., et al., 2012, A&A, 542, A5
DES Collaboration et al., 2017, preprint, (arXiv:1708.01530)
Dawson K. S., et al., 2013, AJ, 145, 10
Eisenstein D. J., et al., 2011, AJ, 142, 72
Elvin-Poole J., et al., 2017, preprint, (arXiv:1708.01536)
Galassi M., Davies J., Theiler J., Gough B., Jungman G., Alken

P., Booth M., Rossi F., 2009, GNU Scientific Library Reference Manual. 3 edn

Gao L., Springel V., White S. D. M., 2005, MNRAS, 363, L66

Garrison L. H., Eisenstein D. J., Ferrer D., Metchnik M. V., Pinto P. A., 2016, MNRAS, 461, 4125

Garrison L., et al., in prep, 2017.

Guo H., et al., 2014, MNRAS, 441, 2398

Harker G., Cole S., Helly J., Frenk C., Jenkins A., 2006, MNRAS, 367, 1039

Hearin A. P., Watson D. F., 2013, MNRAS, 435, 1313

Hearin A. P., Zentner A. R., van den Bosch F. C., Campbell D., Tollerud E., 2016, MNRAS, 460, 2552

Heitmann K., Higdon D., White M., Habib S., Williams B. J., Lawrence E., Wagner C., 2009, ApJ, 705, 156

Heymans C., et al., 2012, MNRAS, 427, 146

Hildebrandt H., et al., 2017, MNRAS, 465, 1454

Hu W., Kravtsov A. V., 2003, ApJ, 584, 702

Hunter J. D., 2007, Computing In Science & Engineering, 9, 90

Jain B., Seljak U., 1997, ApJ, 484, 560

Jee M. J., Tyson J. A., Hilbert S., Schneider M. D., Schmidt S., Wittman D., 2016, ApJ, 824, 77

Leauthaud A., Tinker J., Behroozi P. S., Busha M. T., Wechsler R. H., 2011, ApJ, 738, 45

Leauthaud A., et al., 2017, MNRAS, 467, 3024

Lehmann B. V., Mao Y.-Y., Becker M. R., Skillman S. W., Wechsler R. H., 2017, ApJ, 834, 37

Lemson G., Kauffmann G., 1999, MNRAS, 302, 111

Lewis A., Challinor A., 2011, CAMB: Code for Anisotropies in the Microwave Background, Astrophysics Source Code Library (ascl:1102.026)

Mandelbaum R., et al., 2005, MNRAS, 361, 1287

Mandelbaum R., Seljak U., Cool R. J., Blanton M., Hirata C. M., Brinkmann J., 2006, MNRAS, 372, 758

Mandelbaum R., Slosar A., Baldauf T., Seljak U., Hirata C. M., Nakajima R., Reyes R., Smith R. E., 2013, MNRAS, 432, 1544

Marian L., Smith R. E., Angulo R. E., 2015, MNRAS, 451, 1418

McEwen J. E., Weinberg D. H., 2016, preprint, (arXiv:1601.02693)

Metchnik M. V. L., 2009, PhD thesis, The University of Arizona

More S., 2013, ApJ, 777, L26

More S., van den Bosch F. C., Cacciato M., More A., Mo H., Yang X., 2013, MNRAS, 430, 747

More S., Miyatake H., Mandelbaum R., Takada M., Spergel D. N., Brownstein J. R., Schneider D. P., 2015, ApJ, 806, 2

Murata R., Nishimichi T., Takada M., Miyatake H., Shirasaki M., More S., Takahashi R., Osato K., 2018, ApJ, 854, 120

Navarro J. F., Frenk C. S., White S. D. M., 1997, ApJ, 490, 493

Parejko J. K., et al., 2013, MNRAS, 429, 98

Planck Collaboration et al., 2016, A&A, 594, A13

Prat J., et al., 2017, preprint, (arXiv:1708.01537)

Rozo E., et al., 2016, MNRAS, 461, 1431

Salcedo A. N., Maller A. H., Berlind A. A., Sinha M., McBride C. K., Behroozi P. S., Wechsler R. H., Weinberg D. H., 2017, preprint, (arXiv:1708.08451)

Scoccimarro R., Zaldarriaga M., Hui L., 1999, ApJ, 527, 1

Sheldon E. S., et al., 2004, AJ, 127, 2544

Sheth R. K., Tormen G., 2004, MNRAS, 350, 1385

Singh S., Mandelbaum R., Seljak U., Slosar A., Vazquez Gonzalez J., 2016, preprint, (arXiv:1611.00752)

Sinha M., Garrison L., 2017, Corrfunc: Blazing fast correlation functions on the CPU, Astrophysics Source Code Library (ascl:1703.003)

Tojeiro R., et al., 2014, MNRAS, 440, 2222

Troxel M. A., et al., 2017, preprint, (arXiv:1708.01538)

Wechsler R. H., Zentner A. R., Bullock J. S., Kravtsov A. V., Allgood B., 2006, ApJ, 652, 71

Weinberg D. H., Mortonson M. J., Eisenstein D. J., Hirata C., Riess A. G., Rozo E., 2013, Phys. Rep., 530, 87

White S. D. M., 1994, ArXiv Astrophysics e-prints,

Yoo J., Seljak U., 2012, Phys. Rev. D, 86, 083504

Yoo J., Tinker J. L., Weinberg D. H., Zheng Z., Katz N., Davé R., 2006, ApJ, 652, 26

York D. G., et al., 2000, AJ, 120, 1579

Zehavi I., et al., 2005, ApJ, 630, 1

Zehavi I., et al., 2011, ApJ, 736, 59

Zentner A. R., Hearin A. P., van den Bosch F. C., 2014, MNRAS, 443, 3044

Zentner A. R., Hearin A., van den Bosch F. C., Lange J. U., Villarreal A., 2016, preprint, (arXiv:1606.07817)

Zheng Z., Guo H., 2016, MNRAS, 458, 4015

Zheng Z., et al., 2005, ApJ, 633, 791

Zu Y., Mandelbaum R., 2015, MNRAS, 454, 1161

van Daalen M. P., Schaye J., McCarthy I. G., Booth C. M., Dalla Vecchia C., 2014, MNRAS, 440, 2997

van den Bosch F. C., More S., Cacciato M., Mo H., Yang X., 2013, MNRAS, 430, 725

APPENDIX A: ALTERNATIVE ESTIMATOR FOR GALAXY-GALAXY LENSING

To illustrate the impact of small-scale information on the observables, we show the derivatives of γ_t with respect to HOD parameters, as well as derivatives of an alternative estimator, the Υ estimator (Baldauf et al. 2010), which eliminates lensing information on scales below a given minimum scale R_0. We show the derivatives with respect to HOD parameters and the assembly bias parameter $Q_{\rm env}$ in Figure A1 for $\gamma_t(r)$, $\Upsilon(r; R_0 = 2\,h^{-1}\,{\rm Mpc})$, and $\Upsilon(r; R_0 = 5\,h^{-1}\,{\rm Mpc})$. We note that the scale-dependence of the derivatives of γ_t is quite significant even at $\sim 10\,h^{-1}$ Mpc scales for the derivatives with respect to $n_{\rm gal}$, $M_1/M_{\rm min}$, and $\sigma_{\log M}$, whereas the scale dependence is significantly reduced when using the Υ estimator, except for the assembly bias parameter $Q_{\rm env}$, which exhibits increased scale-dependence at large scales due to the characteristic feature at $8\,h^{-1}$ Mpc due to the use of the $8\,h^{-1}$ Mpc-scale smoothed overdensity.

APPENDIX B: EMULATOR DERIVATIVES

Table B1 lists the fiducial values and derivatives with respect to HOD and cosmological parameters of $\ln b_g$ as a function of radial bin separation for the first 10 radial bins of the full table. Table B2 lists the fiducial values and derivatives with respect to HOD and cosmological parameters of $\ln r_{gm}$ as a function of radial bin separation for the first 10 bins. Table B3 lists the fiducial values and derivatives with respect to cosmological parameters of $\ln b_{nl}$ for the first 10 bins. The full tables are provided as machine-readable ASCII tables in the online supplementary material.

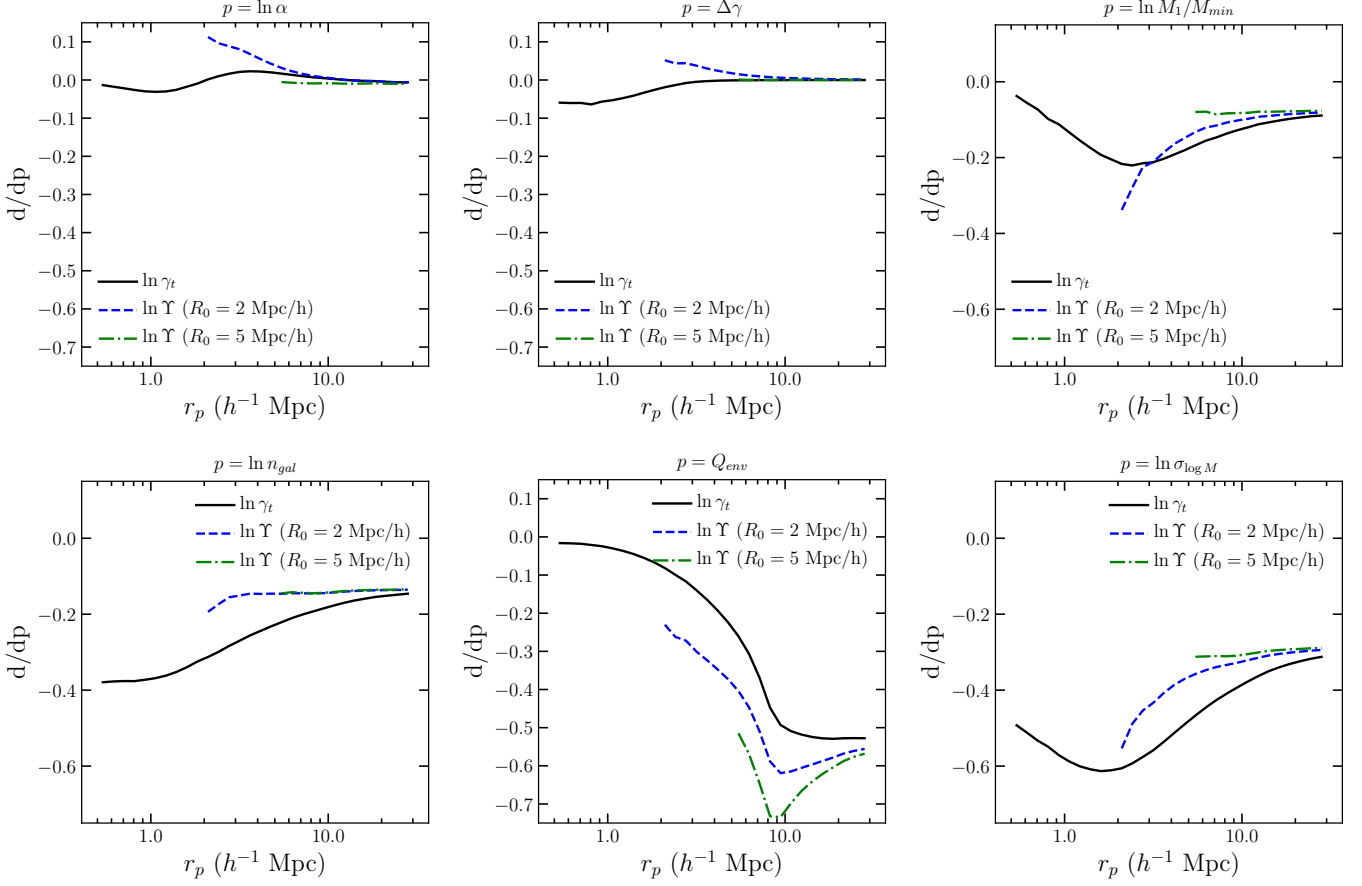This paper has been typeset from a TeX/LaTeX file prepared by the author.

Figure A1. The logarithmic derivatives of various GGL estimators for various HOD parameters.

r_i	r_{i+1}	fiducial	$\partial/\partial \ln n_{\mathrm{gal}}$	$\partial/\partial \ln \sigma_{\log M}$	$\partial/\partial \ln M_1/M_{\min}$	$\partial/\partial \ln \alpha$	$\partial/\partial Q_{\mathrm{env}}$	$\partial/\partial \Delta\gamma$	$\partial/\partial \ln \Omega_M$	$\partial/\partial \ln \sigma_8$
0.0100	0.0112	2.2492	0.6278	-1.0257	-2.5696	-1.2251	-0.0109	-1.7414	0.7138	-0.7489
0.0112	0.0126	1.9929	0.0409	-1.4647	-0.7558	-0.4214	0.0150	-1.4644	-0.5804	-0.7377
0.0126	0.0142	2.4367	-0.3515	-1.2786	-0.8185	-0.5352	-0.0059	-1.8984	0.6373	-0.4411
0.0142	0.0159	2.0490	0.0793	-1.6480	-0.3119	-0.8853	-0.0039	-1.4772	-0.6896	-0.4465
0.0159	0.0179	1.8773	-0.1103	-1.2147	0.1358	-0.7216	-0.0138	-1.6936	-0.3708	-0.7008
0.0179	0.0201	2.0060	0.4151	-1.0349	-0.6610	-0.8776	-0.0071	-1.3927	-1.1537	1.2640
0.0201	0.0226	2.0400	0.3419	-1.2712	-1.0811	-0.9839	-0.0001	-1.8048	0.6078	-0.8494
0.0226	0.0254	1.8421	0.2407	-1.5000	-0.8838	-0.9279	0.0098	-1.7163	0.1132	-0.6852
0.0254	0.0285	1.9109	-0.4028	-1.2632	-1.3304	-0.5197	0.0048	-1.2004	-0.0885	-0.6315
0.0285	0.0320	1.6828	0.2611	-1.5507	-0.6485	-0.6831	-0.0042	-1.1353	-0.2277	-1.4978

Table B1. Fiducial value and derivatives of $\ln b_{\mathrm{g}}$ with respect to HOD and cosmological parameters, as a function of radial bins $[r_i, r_{i+1}]$.

r_i	r_{i+1}	fiducial	$\partial/\partial \ln n_{\rm gal}$	$\partial/\partial \ln \sigma_{\log M}$	$\partial/\partial \ln M_1/M_{\min}$	$\partial/\partial \ln \alpha$	$\partial/\partial Q_{\rm env}$	$\partial/\partial \Delta\gamma$	$\partial/\partial \ln \Omega_M$	$\partial/\partial \ln \sigma_8$
0.0100	0.0112	1.3997	-0.9873	0.7442	2.7071	1.2602	-0.0544	1.7170	-0.3676	2.7523
0.0112	0.0126	1.3034	-0.3727	1.1477	0.8599	0.4457	-0.0943	1.4648	1.1642	2.0329
0.0126	0.0142	1.8720	0.0087	0.9770	0.8789	0.5470	-0.0196	1.9009	-0.5359	2.2829
0.0142	0.0159	1.5348	-0.4251	1.3309	0.3753	0.9039	-0.0148	1.4800	1.0433	1.9450
0.0159	0.0179	1.4248	-0.2047	0.8868	-0.0684	0.7426	0.0067	1.6820	-0.1445	1.5945
0.0179	0.0201	1.6686	-0.7059	0.7138	0.7167	0.9001	-0.0428	1.3826	-0.7254	0.2783
0.0201	0.0226	1.7257	-0.6624	0.9647	1.1101	1.0167	-0.0140	1.7922	-0.0107	0.8995
0.0226	0.0254	1.6475	-0.5777	1.1906	0.9388	0.9686	-0.0239	1.6915	0.2043	0.5866
0.0254	0.0285	1.6799	0.0792	0.9562	1.3640	0.5474	-0.0454	1.1910	0.1123	-0.8946
0.0285	0.0320	1.6269	-0.5976	1.2445	0.6959	0.7063	-0.0243	1.1251	-0.0225	-0.3697

Table B2. Fiducial value and derivatives of $\ln r_{gm}$ with respect to HOD and cosmological parameters, as a function of radial bins $[r_i, r_{i+1}]$.

r_i	r_{i+1}	fiducial	$\partial/\partial \ln \sigma_8$	$\partial/\partial \ln \Omega_M$
0.0100	0.0112	1.3277	-0.4060	-0.1488
0.0112	0.0126	1.4792	-0.2433	0.1631
0.0126	0.0142	1.0111	-1.0000	-0.5412
0.0142	0.0159	1.3407	-0.7627	-0.2355
0.0159	0.0179	1.4737	-0.1833	0.2402
0.0179	0.0201	1.2782	-1.1902	0.4009
0.0201	0.0226	1.2126	0.3140	-0.7944
0.0226	0.0254	1.3546	-0.0298	-0.2946
0.0254	0.0285	1.2875	0.2068	-0.2943
0.0285	0.0320	1.4277	0.7104	0.0258

Table B3. Fiducial value and derivatives of $\ln b_{gL}$ with respect to HOD and cosmological parameters, as a function of radial bins $[r_i, r_{i+1}]$.